Acta Materialia 268 (2024) 119784

Contents lists available at ScienceDirect

Acta Materialia

journal homepage: www.elsevier.com/locate/actamat

# Decoding crystallization behavior of aluminoborosilicate glasses: From structural descriptors to Quantitative Structure – Property Relationship (QSPR) based predictive models

Yingcheng Zhang [a], Marco Bertani [b], Alfonso Pedone [b], Randall E. Youngman [c], Gregory Tricot [d], Aditya Kumar [e], Ashutosh Goel [a,*]

[a] Department of Material Science and Engineering, Rutgers, The State University of New Jersey, Piscataway, NJ 08854, United States
[b] Department of Chemical and Geological Sciences, University of Modena and Reggio Emilia, Via Campi, 103, 41125 Modena, Italy
[c] Science and Technology Division, Corning Incorporated, Corning, NY 14831, United States
[d] Univ. Lille, CNRS, UMR 8516 - LASIRE – Laboratoire de Spectroscopie pour les Interactions, la Reactivite et l'Environnement, F-59000 Lille, France
[e] Department of Materials Science and Engineering, Missouri University of Science and Technology, Rolla, MO 65409, USA

ARTICLE INFO

*Keywords:*
Glass
Crystallization
Structure
Aluminoborosilicate
NMR
MD simulations

ABSTRACT

Successful decoding of structural descriptors controlling the crystallization in multicomponent functional glasses can pave the way for the transition from the *trial-and-error* approach and empirical modeling for glass/glass-ceramic composition design toward more rational and scientifically rigorous Quantitative Structure-Property Relationship (QSPR) based models. However, due to the compositional and structural complexity of multi-component glasses and the longer time and length scales associated with nucleation, the development and validation of QSPR models are still in it's infancy. The work presented in the article is an attempt to leap forward in this pursuit by combining the strengths of experimental and computational materials science to decode the chemo-structural drivers that promote or suppress nucleation and crystal growth in alkali/alkaline-earth aluminoborosilicate glasses leading to the development of a QSPR-based model (powered by MD simulations). The results reveal the following two descriptors that govern the nucleation and crystallization of a particular aluminosilicate phase in the functional glasses: (1) degree of mixing between the $SiO_4$ and $AlO_4$ units, i.e., Si–O–Al linkages, and (2) difference/similarity between the short-to-intermediate range ordering in the glass structure to that of the structure of corresponding crystalline phase. Based on the established composition–-structure–crystallization behavior relationships, a cluster analysis based QSPR model has been developed (and tested) to predict the propensity of nepheline (and anorthite) crystallization in the investigated glasses. The model has been tested on several compositions from the present and previous studies and has successfully predicted the crystallization propensity of all glass compositions, even in cases where previous empirical and semi-empirical models were unsuccessful.

## 1. Introduction

The quest of finding an answer to the question, "why do some glasses crystallize while others do not?" has been a long-standing endeavor [1–3]. Success in this pursuit has significant technological implications, as it will lead to the development of pathways for accelerated design of functional glasses and glass-ceramics with controlled phase assemblages and microstructures. Historically, most of the effort in this direction has been focused on studying simple glass compositions that inherently exhibit a minimal tendency towards devitrification [2,3]. For example, it has been reported that the high glass-forming ability (minimal devitrification tendency) of vitreous $B_2O_3$ and $NaAlSi_3O_8$ is due to the significant differences in the short–to–medium-range ordering in the structure of parent melts and their corresponding isochemical crystalline phases [3]. The rationale behind these investigations is that the knowledge gained from these studies can be used to design multicomponent oxide glasses that are stable against crystallization. While these studies provide a wealth of knowledge, it is difficult to translate it from these simple isochemical systems to design technologically relevant multicomponent non-isochemical systems comprising multiple

* Corresponding author.
*E-mail address:* ag1179@soe.rutgers.edu (A. Goel).

https://doi.org/10.1016/j.actamat.2024.119784
Received 28 May 2023; Received in revised form 16 February 2024; Accepted 20 February 2024
Available online 21 February 2024

framework moieties and non-framework cations. Even the state-of-the-art modeling and simulation approaches are not helpful due to the longer time and length scales associated with the nucleation in glasses than those associated with liquid motion. Recent literature reports efforts to model the nucleation and crystallization behavior of a few simple oxide glass compositions [4–7]. However, modeling the crystallization behavior of a compositionally complex multicomponent glass is still in it's infancy. Due to these reasons, the glass industry tends to align towards developing empirical or semi-empirical (statistical) predictive models based on composition – property relationships (instead of composition – structure – property relationships) and require large volumes of experimental data [8,9]. However, the problem with these empirical models is that owing to their statistical nature, they are only valid (and, thus, applicable) within the *compositional domain* encompassed by the database used to develop, calibrate/fine-tune, and validate them [10]. The outcome of the majority of these models is a "Go/No-Go" based response that predicts whether or not a melt is expected to crystallize during its processing (upon cooling) into the final vitreous product without providing any further insights into the scientific rationale behind that outcome [11,12]. Although helpful during the industrial production of glasses, as a pass/fail test, where the composition of the final product is expected to fluctuate based on the chemical makeup of the batch, as in the case of nuclear waste glasses [13], these models, owing to their non-scientific basis, do not allow the design of novel glass compositions with significantly superior features than the existing ones. On the other hand, considering the infinite number of compositional permutations and combinations that can lead to the formation of glass, parametric evaluations for understanding the glass-forming ability and crystallization tendency of each composition will be an unsurmountable task. Therefore, a combination of models, at different scales, from atomistic through empirical modeling, is required to leap forward in designing glasses over a broad compositional space with minimal or controlled crystallization tendency. However, in the pursuit of developing these atomistic models, one crucial question that needs to be answered is "what are the structural features in a glass that promote or suppress its tendency towards crystallization?" The present article attempts to find an answer to this question using a $Na_2O$–CaO–$Al_2O_3$–$B_2O_3$–$SiO_2$-based glass system designed in the primary crystallization field of nepheline ($NaAlSiO_4$) as a model for multicomponent functional glasses and glass-ceramics. The rationale for selecting the abovementioned glass system has been discussed in the next section. A combination of state-of-the-art experimental and computational techniques has been employed to unearth the structural descriptors controlling the crystallization behavior of these glasses. The results presented in this study are expected to pave the path for developing non-empirical models for the accelerated design of functional glasses.

## 2. Rationale for selecting the nepheline-based glass composition system

### 2.1. Technological relevance of nepheline-based glasses/glass-ceramics

The glass-ceramics designed in the primary phase field of nepheline ($NaAlSiO_4$) gained attention during the 1960s because of their ability to be easily strengthened by the following two techniques: (1) the application of surface compression through the glazing with glasses of lower coefficient of thermal expansion (CTE), and (2) chemical ion exchange treatment involving potassium for sodium exchange. The first glass-ceramic to be used as tableware was based upon a glazed nepheline-based formulation sold by Corning Glass Works under the brand name Centura® [14]. Further, the highest flexural strength (>1450 MPa) ever measured in a bulk glass-ceramic is from chemically strengthened ($Na^+ \rightleftharpoons K^+$) nepheline-based compositions [15]. Since then, the nepheline-based glass-ceramics have been investigated for various functional applications [16–19], the most recent being the development of chemically strengthened transparent and opaque glass-ceramics to develop the touch screens and back covers, respectively, of the next-generation all-glass smartphones and tablets [20,21].

While all the above-discussed applications require controlled nucleation and growth of nepheline-based phases in the glasses, there are several instances in the glass industry where the growth of nepheline and similar aluminosilicate phases (controlled/uncontrolled) is undesirable. As an example, during the fabrication of glass by fusion-draw technique, crystallization in the melt can appear through two different routes: (1) Primary crystallization, i.e., crystallization during the cooling of glass melt due to its high liquidus temperature, and (2) Secondary crystallization, i.e., crystallization in the melt due to its interaction (contamination) with refractory of the isopipe resulting in the change of glass composition. Nepheline has shown up as an unwanted phase in both primary and secondary modes of crystallization during the design and processing of Corning® Gorilla® glass in the $Na_2O$–$Al_2O_3$–$SiO_2$ system [22,23]. From the performance viewpoint, uncontrolled growth of nepheline in the glassy matrix can lead to poor chemical durability of the final glass product. A well-known example of this problem is the lowering of chemical durability of sodium and alumina-rich high-level nuclear waste glasses due to the crystallization of nepheline during the cooling of glass melt in the steel canister [13].

Thus, owing to its significant technological relevance, a deeper understanding of the chemo-structural drivers controlling the crystallization in glasses designed in the primary crystallization field of nepheline is desired to enable the design and development of functional glass/glass-ceramics by materials–by–design approach.

### 2.2. Rationale for the glass composition design

A total of eight glass compositions in the system $Na_2O$–CaO–$Al_2O_3$–$B_2O_3$–$SiO_2$ have been designed and divided into two sets of glasses based on the optical basicity (OB) model. According to the OB model, as proposed by McCloy et al. [24], nepheline precipitation in a glass is expected to be suppressed at low OB (OB <0.55 – 0.57). The hypothesis is that more basic cations are more likely to cause aluminosilicates to precipitate, as they readily donate valence electrons and thus can be readily removed from the covalent glass network. Although the OB model has been reasonably successful in predicting (Go/No-Go) the crystallization propensity of nepheline-based glasses, it has failed in several instances, as shown in our previous studies [25,26]. Therefore, the compositions in the present study have been designed over a range of OB values varying between 0.567 and 0.622 to gain an insight into the chemo-structural drivers controlling the promotion or suppression of nepheline crystallization.

Accordingly, the first series of glasses, labeled as Ca-*x* series, has been designed in the (100-*x*) (25$Na_2O$-25$Al_2O_3$–10$B_2O_3$–40$SiO_2$)-*x*CaO system, where *x* varies between 0 – 15 mol.%. In the Ca-*x* series of glasses, while the OB of baseline glass (OB = 0.590; $x = 0$) is above the threshold range (0.55 – 0.57) proposed by McCloy et al. [24], the addition of CaO ($\Lambda = 1.0$, $\Lambda$ corresponds to the molar basicity of the oxide) to the glass system increases its OB to 0.622 ($x = 15$). Therefore, the glasses in the Ca-*x* series are expected to precipitate nepheline upon slow cooling of the melt. The second series of glasses, labeled NC-*x*, has been designed in the system (25-*x*) $Na_2O$-*x*CaO-17.50$Al_2O_3$–12.50$B_2O_3$–45$SiO_2$, where *x* varies between 0 – 15 mol.%. In the NC-*x* series, the OB of the baseline glass ($x = 0$) is 0.575. The substitution of $Na_2O$ ($\Lambda = 1.1$) by CaO ($\Lambda = 1.0$) results in lowering the OB values of these glasses to 0.567 ($x = 15$). Thus, according to the OB model, the glasses in the NC-*x* series are not expected to precipitate nepheline upon cooling the melt. Here it should be noted that all the glasses in the present study fail the nepheline discriminator (ND) model ($N_{Si} < 0.62$; $N_{Si}$ is the normalized $SiO_2$ concentration in the glass; Table S1) [27]. Therefore, according to the ND model, all the glasses investigated in the present study should crystallize nepheline upon slow cooling of the melt. Further, according to the submixture model

(Figure S1) [28], all the glasses in the Ca-*x* series are expected to crystallize >25 vol.% nepheline, while from the NC-*x* series, the compositions NC-0 and NC-5 are expected to crystallize >25 vol.% nepheline, NC-10 is expected to crystallize between 10 vol.% - 15 vol.% nepheline and composition NC-15 is expected to stay amorphous upon slow cooling from the melt. The readers are referred to Ref. [13] to read more about the abovementioned predictive models. Table S1 presents the batched molar compositions of the glasses investigated in the present study along with their OB and $N_{Si}$ values.

## 3. Experimental and computational methodology

### 3.1. Glass synthesis

The glasses were synthesized by the melt-quench technique, as discussed in our previous articles [29,30]. In brief, a batch comprising high purity (>99+%) oxides and carbonates corresponding to 120 g glass was calcined (1000 °C; 3 h) and melted (1500 – 1620 °C; dwell time: 1 h) in Pt-Rh crucibles. The melts were poured on a copper plate and air-quenched to room temperature. The amorphous nature of the as-quenched samples was confirmed by X-ray diffraction (XRD; PANalytical – X'Pert Pro; Cu $K_\alpha$ radiation; 2θ range: 10°–90°; step size: 0.001° $s^{-1}$). The experimental composition of all the glasses has been analyzed by inductive coupled plasma–optical emission spectroscopy (ICP-OES; PerkinElmer Optima 8300). Table S2 presents a comparison between batched and experimental compositions (wt.%). As evident, the batched and experimental compositions of the glasses are in good agreement with each other, with minimal $B_2O_3$ volatility observed from the melts. Further, the density of glasses, as measured by Archimedes' method (using D-limonene; 3 samples per composition), is presented in Table S1.

### 3.2. Structure of glasses

#### 3.2.1. Raman spectroscopy

Raman spectra of the glasses were acquired at room temperature using a Renishaw inVia Raman spectrometer equipped with a confocal microscope in the backscattered geometry. The light was directed normally to a smooth sample surface in backscattering geometry and focused to a spot at 20× magnification. The flat surface of the samples was then excited by a diode laser with a wavelength of 532 nm at an output power of around 10 mW, and the backscattered light was analyzed with diffraction grating of 1800 grooves/mm. The unpolarized spectra were recorded from 300 $cm^{-1}$ to 1600 $cm^{-1}$. Integration time on each sample was 100 s with an exposure time of 10 s $cm^{-1}$ with 10 accumulations per scan. A correction factor was applied to the spectra to account for the dependence of the scattered intensity on frequency [31,32]. The obtained Raman intensities were later baseline corrected and normalized to the total integrated area.

#### 3.2.2. 1D and 2D solid state nuclear magnetic resonance (ss NMR) spectroscopy

The $^{11}B$, $^{23}Na$, $^{27}Al$ magic angle spinning – nuclear magnetic resonance (MAS NMR) spectra were obtained using commercial spectrometers (VNMRs or DD2 Agilent) employing a 3.2 mm MAS NMR probe (Agilent). After being crushed in an agate mortar and packed into 3.2 mm zirconia rotors, the samples were spun at rotation frequencies ($\nu_{rot}$) of 22 kHz for $^{23}Na$, $^{27}Al$ MAS NMR, and 20 kHz for $^{11}B$ MAS NMR spectroscopy. $^{23}Na$ MAS NMR experiments were conducted at 16.4 T for Ca-*x* series and 11.7 T (132.19 MHz resonance frequency) for NC-*x* series with a 0.6 μs (~π/12 tip angle) pulse width. The recycle delays were set to 2 s, and a range of 400–1000 acquisitions was co-added. $^{11}B$ and $^{27}Al$ MAS NMR data were collected at 16.4 T (224.52 and 182.34 MHz resonance frequency, respectively). The $^{11}B$ and $^{27}Al$ NMR data acquisition incorporates a 4 s recycle delay, short rf pulses (0.6 μs) corresponding to a π/12 tip angle, and signal averaging of 400 to 1000 scans. The $^{29}Si$ MAS NMR experiments were recorded at 9.4 T (79.53 MHz) using 7.0 mm zirconia rotors spinning at a $\nu_{rot}$ of 5 kHz. The data were collected with a 5.0 μs (π/2 tip angle) pulse length, 256 scans and a recycle delay of 180 s. The acquired spectra were processed with minimal apodization and referenced to aqueous boric acid (19.6 ppm), aqueous NaCl (0.0 ppm), aqueous aluminum nitrate (0.0 ppm) and tetramethylsilane (0.0 ppm). DMfit was used to perform the fitting of the obtained MAS NMR spectra [33]. The "Czjzek" model [34] was utilized for $^{27}Al$ and $^{23}Na$ MAS NMR spectra to account for the distributions in the quadrupolar coupling parameters. Satellite transition spinning sidebands have been incorporated in the fitting of $^{27}Al$ MAS NMR data to better estimate the fraction of $AlO_4$ and $AlO_5$ units. 2nd-order quadrupolar lineshapes and mixed Gaussian/Lorentzian peaks were used to fit the 3- and 4-fold coordinated boron resonances in the $^{11}B$ MAS NMR data, respectively. The $N_4$ ($= \frac{BO_4}{BO_3+BO_4}$) fraction was calculated from the fitted peaks, with a small correction applied to account for the overlapping satellite transition spinning side band of four-fold coordinated boron.

$^{11}B$ triple quantum magic-angle spinning (3QMAS) NMR spectra were collected using a hypercomplex 3QMAS pulse sequence with a Z filter [35]. The solid 3π/2 and π/2 pulse widths were optimized to 3.2 and 1.2 μs, respectively. A lower power π/2 pulse width of 20.0 μs was used as the soft reading pulse, after a delay of 50 μs, for the Z filter. The data were typically collected using 48 to 168 acquisitions at each of 160 $t_1$ points, with a recycle delay of 1 s and sweep widths of 100 kHz in both dimensions. The $^{11}B$ 3QMAS NMR data were processed using commercial software, without apodization, and referenced to 1 M boric acid at 19.6 ppm.

3QMAS NMR spectra were collected for $^{23}Na$ using the same pulse sequence as above, but with calibrated 3π/2 and π/2 pulse widths of 3.6 μs and 1.3 μs, and Z-filtering with a soft reading pulse of 20 μs and storage delay of 45.5 μs. $^{23}Na$ 3QMAS NMR experiments involved signal averaging of 480 scans at each of 36 to 64 $t_1$ delay values, with a recycle delay of 0.5 s, a 2nd-dimensional dwell time of 10 μs, corresponding to an isotropic sweep width of 100 kHz, and processing without apodization. $^{23}Na$ 3QMAS NMR data were referenced using an external aqueous NaCl standard at 0.0 ppm. Isotropic projections for both $^{11}B$ and $^{23}Na$ 3QMAS NMR data were fit to a series of Gaussian functions using commercial software.

$^{27}Al$ 3QMAS NMR data were also collected using the same NMR pulse sequence as described above, incorporating 3π/2 and π/2 pulse widths of 2.8 μs and 1.1 μs, and Z-filtering with a soft reading pulse of 15 μs and storage delay of 45.5 μs (one rotor cycle). $^{27}Al$ 3QMAS NMR data were typically collected with signal averaging of 48 acquisitions at each of 80 delay values, using a recycle delay of 0.5 s. Sweep widths in both dimensions were set to 100 kHz. In the case of $^{27}Al$ 3QMAS NMR data, processing included 100 and 50 Hz apodization in the MAS and isotropic dimensions, respectively, to aid in confirmation of weak signals from $AlO_5$ polyhedra, as will be discussed below.

Further, to understand the structure of the investigated glasses at the intermediate-range order, the Al/Si and B/Si mixing in the glass structure has been analyzed using the dipolar heteronuclear multiple quantum coherence (D-HMQC) NMR sequence [36,37]. This NMR sequence is used to produce a 2D map in which correlation signals indicate spatial proximity between the two involved nuclei. In the experiments reported here, the recoupling times have been set up to short values that only allow interaction between the closest nuclei. Therefore, the spatial proximity highlighted by our experiments can be safely discussed in terms of chemical connectivity in the glass structure [38]. The 2D $^{27}Al/^{29}Si$ D-HMQC experiments were performed at 9.4 T on a 4 mm probe with a $\nu_{rot}$ of 8 kHz. The 1024 × 24 acquisition points were recorded under rotor-synchronized condition with π pulses of 20 μs and 10 μs on the $^{27}Al$ and $^{29}Si$ channels, respectively. Each direct slice was acquired with 8192 transients, a recycle delay of 0.25 s, and a 16 kHz ($=2*\nu_{rot}$) $SR4_1^2$ recoupling scheme of 2 × 1.5 ms. The $^{11}B/^{29}Si$ D-HMQC experiments were performed at 18.8 T on a 3.2 mm probe with a $\nu_{rot}$ of

20 kHz. The 1024 × 20 acquisition points were recorded under rotor-synchronized condition with π pulses of 22 μs and 7 μs on the $^{11}B$ and $^{29}Si$ channels, respectively. Each slice was acquired with 2048 transients, a recycle delay of 1 s, and a 40 kHz (=2*$\nu_{rot}$) $SR4_1^2$ recoupling scheme of 2 × 2 ms.

#### 3.2.3. Molecular dynamic (MD) simulations

The NMR spectroscopy results have been complemented and augmented by the MD simulations. The MD simulations have been performed using the DL_POLY2.14 package [39], describing the interatomic interactions between ionic pairs through shell model potentials with parameters reported in Table S3 [40–42]. The melt-quench approach has been used to generate models containing ~3500 atoms (three replicas for each composition) [43]. The exact number of atoms and box dimensions are reported in Table S4.

The initial configurations were generated by randomly placing the number of atoms in a cubic box, whose dimensions were constrained by the experimental densities. The systems were heated and held at 3200 K for 100 ps in the *NVT* ensemble, ensuring suitable melting of the samples. The liquids were then cooled to 300 K at a cooling rate of 5 K/ps. The resulting glass structures were subjected to a final equilibration run of 200 ps.

The equation of motion has been integrated using the leap-frog algorithm with a time step of 0.2 fs. The kinetic energy (temperature) of the shells has been controlled by applying velocity scaling at every step during the quenching of the melt. Coulomb interactions were calculated by the Ewald summation method with a cut-off of 8 Å, whereas short range cut-off values of 7.5 Å were used.

### 3.3. Crystallization during slow cooling of glass melts

#### 3.3.1. Liquidus temperature

The liquidus temperature ($T_L$) of the investigated glasses was measured using the gradient furnace method as per the standard ASTM C829 – 81 [44]. ~30 g powdered glass with particle size varying between 300 μm to 425 μm was loaded into a Pt-Rh boat (15 cm × 0.5 cm bottom; 0.6 cm height; 16.2 cm × 0.8 cm top) and inserted into a muffle tube gradient furnace (Orton GTF −1616STD - G). A tentative range of liquidus temperature was estimated for each composition by locating the melting curve obtained from the differential scanning calorimetry (DSC). Based on the estimated temperature range, the Pt-Rh boat was heated in the furnace to the point where the samples at the hot end of the boat melted entirely while those at the cold end of the boat remained unmelted. The boat was kept in the gradient furnace for at least 24 h for a complete heating cycle, after which the boat was taken out from the furnace and cooled in air. The amorphous nature of the samples from the hot end and the crystalline nature of the samples from the cold end was confirmed by the XRD. The samples were then observed under an optical microscope by moving along the boat from the hot-to-cold end. The length between the hot end to the point where the first crystal was observed under the optical microscope was measured, and the $T_L$ was determined by correlating that value with the location vs. temperature curve of the gradient furnace. Finally, the samples from the cold-end of the platinum boat were passed through XRD to identify the crystalline phase at the liquidus temperature.

#### 3.3.2. Crystallization behavior during cooling of glass melts

The crystallization behavior of the glasses during cooling from melt stage has been studied following the schedule of canister centerline cooling (CCC; Table S5) tests for the legacy nuclear waste glasses in the United States [25]. Around 20 gs of glass frits were loaded in boats made of Pt sheets and covered by lids made of the same sheets. The platinum boats were then loaded into an electric furnace and heated in the 1300 to 1400 °C range, depending on the $T_L$ of the corresponding glass, to achieve homogeneous melts. The samples were then allowed to cool down according to the CCC schedule. The CCC tests were performed in triplicate to account for the uncertainty in the results. The glass-ceramics obtained from the CCC experiments were then crushed into powders with particle size <45 μm for quantitative phase analysis using XRD Rietveld refinement. 10 wt.% corundum (NIST SRM 676a) was used as an internal standard. XRD analysis of the samples was performed on PANalytical – X'Pert Pro-XRD with a Cu-$K_\alpha$ tube (45 kV and 40 mA, in the 2θ range of 10 – 90° with 0.001° 2θ step size, and dwell time of 5.7 s) and the quantitative phase analysis was performed using the whole pattern fitting (WPF) Rietveld analysis in the MDI Jade software.

## 4. Results

### 4.1. Structure of glasses - experimental

#### 4.1.1. Raman spectroscopy

Fig. 1 presents the baseline corrected and normalized Raman spectra of glasses investigated in the present study. For the convenience of analysis, the Raman spectra have been divided into the following three regions: low frequency (300 - 850 $cm^{-1}$), mid-frequency (850 - 1200 $cm^{-1}$), and high frequency (1200 - 1600 $cm^{-1}$). A point-by-point summary of the structural changes deciphered from the Raman spectra of glasses as a function of their chemical composition has been presented below.

1. In the low-frequency region, the Raman spectra of both the series of glasses exhibit peaks centered at 490 $cm^{-1}$, 570 $cm^{-1}$, 760 $cm^{-1}$, and 840 $cm^{-1}$. The band located at 490 $cm^{-1}$, known as the D1 band, can be assigned to the vibration mode of T–O–T (T: Si, Al) bridging oxygens in four-membered rings [45,46]. The intensity of this band decreases with increasing CaO concentration in Ca-*x* series (Fig. 1a), indicating a decrease in the network connectivity, possibly due to an increasing amount of network modifier ($Ca^{2+}$) in the glass structure. However, a similar band intensity change is not observed in the NC-*x* glasses (Fig. 1b).
2. The band at 570 $cm^{-1}$ can be assigned to breathing vibrations of three-membered aluminosilicate rings associated with one or two Al atoms (D2 band) [45–47], or the breathing mode of reedmergnerite-like borosilicate units where boron exists as $BO_4$ tetrahedra and is associated with three $SiO_4$ units [10]. Based on the results of $^{11}B$ MAS NMR spectroscopy (discussed in the next section), the fraction of $BO_4$ units in the Ca-*x* glasses is less than 2 %, thus negating the possibility of formation of reedmergnerite units. Therefore, the band at 570 $cm^{-1}$ has been assigned to the three-membered aluminosilicate rings whose intensity remains constant with increasing CaO in both the Ca-*x* and NC-*x* series of glasses.
3. A broad band between 700 and 800 $cm^{-1}$ with a peak maximum of around 760 $cm^{-1}$ exists in the Raman spectra of both the series of glasses. A subtle decrease in the band's intensity can be observed with increasing CaO concentration in the Ca-*x* series. However, minimal impact in the band's intensity is observed for the NC-*x* series of glasses. A precise assignment of this broad feature is hard to accomplish due to the strong overlapping of bands corresponding to T–O–T bending modes or T–O stretching vibrations involving oxygen vibrations in the T–O–T (T: Si, Al) planes in aluminosilicate glasses [48–50], and the breathing mode of chain-type metaborate groups (at 720 $cm^{-1}$) along with the breathing motion of $BO_4$ tetrahedra in six-membered diborate rings (at 770 $cm^{-1}$) in borosilicate glasses [32], Thus, a subtle decrease in the intensity of this band in the Ca-*x* glasses is difficult to decipher. Finally, the absence of a band around 808 $cm^{-1}$ in the low-frequency region implies the absence of a boroxol ring-type structure [32,51], thus, suggesting a high degree of mixing between the borate and silicate units.
4. In the mid-frequency region, the Raman spectra of both the series of glasses show a broad, featureless band between 850 $cm^{-1}$ to 1100 $cm^{-1}$, with maximum intensity at ~1000 $cm^{-1}$, corresponding to the

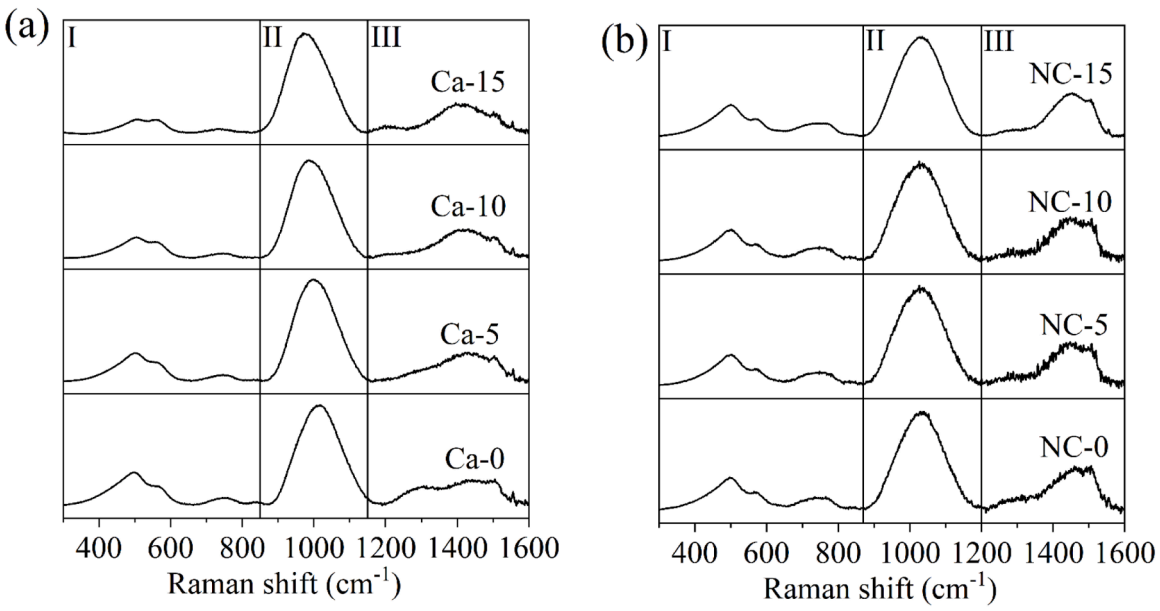


**Fig. 1.** Raman spectra of (a) Ca-*x* series and (b) NC-*x* series of glasses.

stretching T–O–T (T: Si, Al) vibrations in the glass network [32,50,52]. In the Ca-*x* series, an increase in CaO concentration results in a gradual shift of this band towards lower frequency and increased intensity (Figure S2a), suggesting a decrease in the degree of polymerization in the glass network. This observation can be explained based on the shift of the composition system from a metaluminous (Ca-0; $Na_2O + CaO/Al_2O_3 = 1$) to peralkaline ($Na_2O + CaO/Al_2O_3 > 1$) regime, thus, resulting in the possible generation of NBOs in the network. On the other hand, the alkali/alkaline-earth oxide–to–$Al_2O_3$ ratio in the NC-*x* series remains constant with an increase in $CaO/Na_2O$. Therefore, ideally, the degree of polymerization in the network of NC-*x* glasses is not expected to change. The experimental results agree with the prediction as a change in the $Na_2O/CaO$ in NC-*x* glasses has minimal impact on the position and intensity of the band in the mid-frequency region (Figure S2b). Here it should be noted that we are not completely negating the formation of NBOs in the NC-*x* series of glasses as the presence of $Ca^{2+}$ with high ionic field strength is expected to induce heterogeneity in the glass structure, thus, leading to the formation of NBOs [53,54]. However, the concentration of NBOs formed due to the substitution of $Ca^{2+}$ for $Na^+$ in these glasses, if any, is low enough not to induce any changes in the shift of Raman spectra. A quantitative estimation of NBOs in the investigated glasses, based on the $^{11}B$ and $^{27}Al$ MAS NMR results, has been discussed in Section 4.1.2.

5. The high-frequency region shows the bands corresponding to stretching vibrations of asymmetric $BO_2O^-$ metaborate groups [32,55,56]. In the Ca-*x* series, the Raman spectra of Ca-free glass (Ca-0) shows two broad bands centered at ~1300 $cm^{-1}$ and 1440 $cm^{-1}$, along with one sharp peak located at 1510 $cm^{-1}$. With the addition of CaO, the band at 1300 $cm^{-1}$ disappears while the 1440 $cm^{-1}$ band shifts to 1400 $cm^{-1}$ with increased intensity. The band at 1510 $cm^{-1}$, however, remains identical. The assignment for the 1300 $cm^{-1}$ peak is attributed to loose $BO_3$ units, i.e., $BO_3$ units that do not participate in geometrically constrained superstructural units [32,57]. Therefore, a decreasing intensity of the 1300 $cm^{-1}$ peak with increasing CaO content in Ca-*x* glasses indicates a decrease in the non-ring $BO_3$ units. The bands at 1400 $cm^{-1}$ and 1440 $cm^{-1}$ are attributed to asymmetric $BO_3$ units (with NBOs) attached with $BO_3$ and $BO_4$ units, respectively, while the 1520 $cm^{-1}$ band corresponds to the metaborate ring structure [58]. The presence of these bands confirms the presence of NBOs in the borate network, in agreement with the $^{11}B$ 3QMAS NMR spectroscopy results (discussed in Section 4.1.2.2). Further, a small band corresponding to symmetric $B–O^-$ stretching vibrations in pyroborate $[B_2O_5]^{4-}$ units appears at ~1210 $cm^{-1}$ in glasses with high CaO (Ca-10 and Ca-15) [59]. Similar to the Ca-*x* glasses, the Raman spectra of the NC-*x* glasses in the high-frequency region depict broad bands at 1290 and 1460 $cm^{-1}$ along with a sharp peak centered at 1510 $cm^{-1}$. However, only a slight decrease in the band's intensity at 1290 $cm^{-1}$ is observed with increasing $CaO/Na_2O$, while the other two bands remain the same.

### 4.1.2. Solid-state nuclear magnetic resonance (ss NMR) spectroscopy

*4.1.2.1. Sodium environment in the glasses.* Figures S3 presents the $^{23}Na$ MAS NMR spectra of the Ca-*x* (Figure S3a) and NC-*x* (Figure S3b) series of glasses, while Table S6 presents the isotropic chemical shift ($\delta_{CS}$), quadrupolar coupling constant ($C_Q$), and full width half maxima (FWHM), as obtained from the fitting of the spectra. Due to the complexity associated with the fitting of the $^{23}Na$ MAS NMR spectra (the Czjzek model, while widely used for simulation of these quadrupolar lineshapes, is unable to accurately capture the full shape of these resonances), the $^{23}Na$ 3QMAS NMR spectra have been used to evaluate the Na environment in the structure of the investigated glasses.

Figures S4 and S5 present the $^{23}Na$ 3QMAS NMR spectra of glasses from Ca-*x* and NC-*x* series, respectively. The $^{23}Na$ 3QMAS NMR spectra of all glasses show a dominant chemical shift distribution with broadening due to the quadrupolar coupling. This indicates a wide distribution of environments around $Na^+$, a characteristic feature of glasses. The $\delta_{CS}$ and quadrupolar coupling products ($P_Q$) have been calculated by determining the frequencies corresponding to the shifts of the MAS projections ($\delta_{MAS}$) and the isotropic projections ($\delta_{ISO}$) via Eqs. (1) and (2) [60]:

$$\delta_{CS} = \frac{10}{27}(\delta_{MAS}) + \frac{17}{27}(\delta_{ISO}) \quad (1)$$

$$P_Q = (\delta_{ISO} - \delta_{MAS})^{1/2} \times 5.122 \times 0.1851018 \quad (2)$$

The two constants in Eq. (2) are determined by the nuclear spin of $^{23}Na$ ($f(I) = 5.122$ for $I = 3/2$) and the Larmor frequency utilized for the experiments, respectively. The results of the corresponding analysis have been presented in Table 1. The $\delta_{CS}$ for Ca-*x* series increases from −5.1 ppm to −2.1 ppm with increasing CaO content, while it decreases

**Table 1**
$^{23}$Na isotropic chemical shift ($\delta_{CS}$), quadrupolar coupling product ($P_Q$), and Na–O bond distance for the investigated glasses as derived from the center of gravity of the resonance in $^{23}$Na 3QMAS NMR spectra and calculations described in the text.

| | $\delta_{CS}$ (ppm) (± 0.3 ppm) | $P_Q$ (MHz) (± 0.1 MHz) | *d* (Na–O) |
|---|---|---|---|
| Ca-0 | −5.1 | 1.61 | 2.69 |
| Ca-5 | −4.0 | 1.61 | 2.67 |
| Ca-10 | −3.2 | 1.64 | 2.66 |
| Ca-15 | −2.1 | 1.82 | 2.64 |
| NC-0 | −5.5 | 2.59 | 2.70 |
| NC-5 | −6.9 | 2.56 | 2.72 |
| NC-10 | −7.7 | 2.54 | 2.73 |
| NC-15 | −9.7 | 2.55 | 2.76 |

from −5.5 ppm to −9.7 ppm in the NC-*x* series. The $P_Q$ increases from 1.61 MHz to 1.82 MHz in the Ca-*x* series, while it remains constant (~2.55 MHz) in the NC-*x* series with increasing CaO concentration.

Further, the values of Na–O bond distance, *d*(Na–O), calculated using Eq. (3) [61,62], are presented in Table 1.

$$\delta_{CS} = -64.4 \times d(Na-O) + 168.3 \quad (3)$$

The *d*(Na–O), generally exhibits an opposite trend with increasing CaO concentration in the two series of glasses. While the *d*(Na–O) decreases from 2.69 Å to 2.64 Å in Ca-*x* series, the value increases from 2.70 Å to 2.76 Å in the NC-*x* series. A subtle decrease in *d*(Na–O) with increasing CaO in the Ca-*x* glasses may be attributed to the transition in the role of $Na^+$ from the charge compensator (of $AlO_4^-$) to the network modifier (creating NBOs) [54,63,64]. Since Ca-0 glass is metaluminous, all the aluminum is expected to exist in four-coordination being charge compensated by $Na^+$. With the addition of CaO to the system, some $AlO_4$ units will be charge-compensated by $Ca^{2+}$, thus, making a few $Na^+$ available to create NBOs and/or four-fold coordinated boron in the glass network. On the contrary, an increase in *d*(Na–O) from 2.70 Å to 2.76 Å with increasing CaO/$Na_2O$ in the NC-*x* series suggests more of the oxygens around $Na^+$ are bridging oxygens instead of NBOs.

*4.1.2.2. Borate environment in the glasses.* The $^{11}$B MAS NMR spectra of all the investigated glasses are presented in Fig. 2. In general, the $^{11}$B MAS NMR spectra of all the investigated glasses are characterized by the presence of two broad peaks: one between 10 ppm to 20 ppm corresponding to trigonal borate units, and the second small peak centered at ~2 ppm corresponding to tetrahedral borate units. As discussed above, considering the metaluminous nature of Ca-0 glass, the $Na^+$ are expected to charge-compensate $AlO_4^-$ units. Therefore, boron in this glass is expected to be primarily three-coordinated. The results of $^{11}$B MAS NMR spectroscopy (Fig. 2a) are in good agreement with the prediction as the fraction of $N_3$ ($=\frac{BO_3}{BO_3+BO_4}$) units in the Ca-0 glass is 98.6 % (Table 2; please refer to Tables S7 and S8 for the fitting parameters of the MAS and 3QMAS NMR spectra). The addition of CaO to the Ca-*x* glasses does not significantly impact their boron coordination as the $N_4$ fraction in these glasses is ≤ 3 %. This is intriguing as adding CaO shifts the composition system from metaluminous to peralkaline. Therefore, one should expect the $BO_3 \rightarrow BO_4$ conversion to be facilitated. However, as has been shown by Wu and Stebbins [54], the high field strength cations, e.g., $Ca^{2+}$, favor the formation of highly charged NBOs, over the lower charged bridging oxygens that form linkages such as $SiO_4$–$BO_4$, thus, shifting the Eq. (4) to the left. The resulting greater concentration of negative charge helps stabilize the local coordination environment of the high-field strength cation.

$$BO_{3/2} + SiO_{3/2}O^- = [BO_{4/2}]^- + SiO_{4/2} \quad (4)$$

In the case of NC-*x* glasses (Fig. 2b), the $N_4$ fraction in NC-0 glass is 23 %, gradually decreasing to 10 % (in Ca-15) with increasing CaO content at the expense of $Na_2O$. These results can also be explained by the affinity of $Ca^{2+}$ to associate with highly charged NBOs (instead of bridging oxygens) and the preference of $Na^+$ to charge-compensate $AlO_4^-$ over $BO_4^-$ [53,54,63].

Based on the results of $^{11}$B, $^{27}$Al MAS NMR spectroscopy (discussed in Section 4.1.2.3) and the chemical composition of the glasses, we have estimated the number of NBOs on silicate and borate units in the glass network using equations (5–6),

$$f_{M,leftover} = f_M - f_{Al} - f_B \times N_4 \quad (5)$$

$$\langle NBO_{Si,B} \rangle = \frac{f_{M,leftover}}{f_{Si} + f_B \times N_3} \quad (6)$$

where M represents the total amount of effective charge that $Na^+$ and $Ca^{2+}$ can provide ($f_M = f_{Na} + 2{*}f_{Ca}$); $f_i$ refers to the atomic fraction of the element *i* in the glass. It should be noted here that these calculations are based on the following assumptions: (1) There are negligible amounts of NBO on Al units, and (2) NBOs are formed on $SiO_4$ and $BO_3$ units. As evident from Table 2, the fraction of NBOs on the silicate and borate units increases from 0 to 0.585 with increasing CaO content in Ca-*x* glasses, while there is an incremental increase from 0.144 to 0.185 in NC-*x* glasses.

Figs. 2(c) and 2(d) present the isotropic projections of the $^{11}$B 3QMAS NMR spectra of the glasses from the Ca-*x* and NC-*x* series, respectively. The high-resolution isotropic projections from the $^{11}$B 3QMAS NMR spectra are free of second-order quadrupolar broadening and, therefore, help obtain a detailed insight into the type and concentration of trigonal borate units present in the glass structure, as presented in Table 2. In the Ca-*x* series, the peak representing three coordinated boron has been fitted with two Gaussian peaks centered at isotropic shifts of 19.3 ppm and 20.6 ppm for the CaO-free sample (Ca-0). Considering its metaluminous nature, no NBOs are expected either in the silicate or borate network of the glass Ca-0. Thus, the two peaks have been assigned to non-ring and ring $BO_3$, respectively [65,66]. With an increase in CaO concentration in the Ca-*x* series, it is observed that the isotropic $BO_3$ peak in the 3QMAS NMR spectra shifts towards higher frequency (deshielding of the nuclei), suggesting the formation of NBOs (Table 2) [66]. This agrees with the above-discussed network-modifying role of CaO in the investigated glasses leading to the formation of NBOs in both silicate and borate network, as evidenced by the appearance of metaborate-related bands in the Raman spectra. Accordingly, a new Gaussian curve with an isotropic peak position at 22.1 ppm, corresponding to the asymmetric trigonal borate units with one NBO, has been added to the spectra.[1]

The isotropic projections of the $^{11}$B 3QMAS NMR spectra of NC-*x* glasses (Fig. 2d) do not show any significant shift with increasing CaO/$Na_2O$, unlike Ca-*x* glasses. Therefore, the spectra have been fitted with only two Gaussian curves – one centered at 20.6 ppm and another at 19.3 ppm, attributed to the $BO_3$ ring and non-ring units, respectively. A small tail at the spectra's low-frequency side has been considered an artifact – likely a partially overlapping spinning sideband. Here it needs to be emphasized that the formation of NBOs upon increasing CaO/$Na_2O$ in the NC-*x* glasses cannot be negated, as has been discussed above. However, the concentration of NBOs formed in these glasses as a function of CaO/$Na_2O$ is low enough not to induce a detectable shift in the $^{11}$B 3QMAS NMR spectra (Table 2).

Also, it must be emphasized that despite the significant increase in the fraction of asymmetric $BO_3$ units in the Ca-*x* glasses, the fraction of ring $BO_3$ units increased from 30.6 % to 48.2 %, while the non-ring $BO_3$ units decreased from 69.4 % to 21.3 % (Table 2). These results are consistent with those from Raman spectroscopy, where 'loose' $BO_3$ units

[1] Based on the chemical composition of the Ca-*x* system, the formation of $BO_3$ units with two NBOs is unlikely due to the insufficient amount of network modifiers in the glass network.

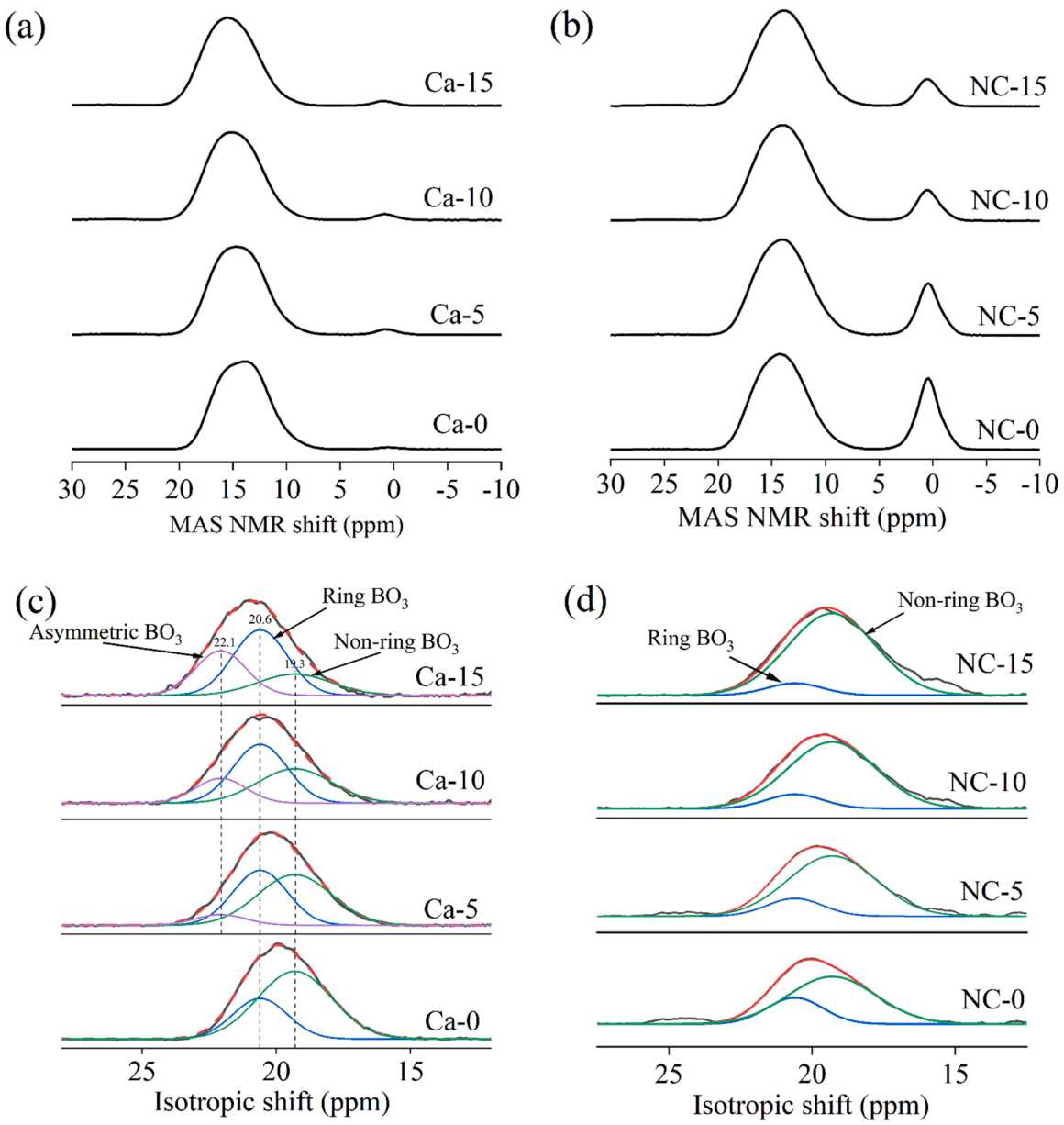


**Fig. 2.** $^{11}$B MAS spectra of (a) Ca-*x* and (b) NC-*x*, and $^{11}$B 3QMAS NMR isotropic projections of (c) Ca-*x* and (d) NC-*x* series of glasses.

**Table 2**
Borate and aluminate speciation as deduced from $^{11}$B MAS, 3QMAS and $^{27}$Al MAS NMR spectroscopy. The values of asymmetric, ring, and non-ring $BO_3$ species are reported as fractions of the total trigonal boron ($N_3$). The fraction of NBOs has been estimated using Eqs. (5) and (6).

| | $N_3$ (%) (± 0.2) | $N_4$ (%) (± 0.2) | Asymm. $BO_3$ (%) (± 2) | Ring $BO_3$ (%) (± 2) | Non-ring $BO_3$ (%) (± 2) | $Al^{[4]}$ (%) (± 1) | $Al^{[5]}$ (%) (± 1) | $f_{M,\text{leftover}}$ | $<NBO_{Si,B}>$ |
|---|---|---|---|---|---|---|---|---|---|
| **Ca-0** | 98.6 | 1.4 | 0 | 30.1 | 69.9 | 99 | 1 % | −0.001 | 0* |
| **Ca-5** | 97.2 | 2.8 | 6.5 | 46.1 | 47.3 | 99 | 1 % | 0.030 | 0.168 |
| **Ca-10** | 97.1 | 2.9 | 17.8 | 49.4 | 32.8 | 98 | 2 % | 0.063 | 0.364 |
| **Ca-15** | 97.7 | 2.3 | 30.5 | 51.9 | 17.6 | 98 | 2 % | 0.098 | 0.585 |
| **NC-0** | 77.0 | 23.0 | 0 | 26.2 | 73.8 | 99 | 1 % | 0.030 | 0.144 |
| **NC-5** | 82.7 | 17.3 | 0 | 15.8 | 84.2 | 98 | 2 % | 0.034 | 0.163 |
| **NC-10** | 88.8 | 11.2 | 0 | 12.0 | 88.0 | 97 | 3 % | 0.038 | 0.182 |
| **NC-15** | 90.0 | 10.0 | 0 | 8.6 | 91.4 | 96 | 4 % | 0.038 | 0.185 |

* This value is set to be 0 due to the negative NBO amounts.

have been found to decrease with increasing CaO concentration in the Ca-*x* glasses. Such changes suggest a decrease in silicon-boron mixing in the glass network, as non-ring $BO_3$ are known to undergo random mixing with the silicate network, while ring $BO_3$ units tend to connect with borate groups only [67]. On the contrary, an increase in CaO concentration in NC-*x* glasses decreases the fraction of ring-$BO_3$ units (from 26.2 % to 8.6 %), while the non-ring $BO_3$ fraction increases from 73.8 % to 91.4 %. Further, considering a possible peak overlap between the ring $BO_3$ and the asymmetric $BO_3$ units, the decreasing trend of ring $BO_3$ units in the NC-*x* series could be more significant. Thus, a higher degree of B/Si mixing is expected when increasing CaO concentration in the NC-*x* glasses.

To confirm the inferences about the degree of mixing in the borate and silicate network, as derived from the 1D $^{11}$B MAS NMR spectroscopy of the investigated glasses, D-HMQC $^{11}$B/$^{29}$Si and $^{27}$Al/$^{29}$Si MAS NMR spectroscopy has been performed on the selected glass compositions. Table 3 lists the NMR signatures of the $^{29}$Si($^{11}$B) and $^{29}$Si($^{27}$Al) species. Fig. 3a presents the $^{11}$B-$^{29}$Si 2D correlation maps of glasses Ca-0, Ca-15, NC-0, and NC-15, accompanied by the $^{11}$B and $^{29}$Si normalized projections in the horizontal and vertical axis, respectively. The maps show that all the glasses exhibit strong correlation signals indicating a significant interaction between the borate and silicate network. Further, Fig. 3b shows the non-normalized $^{11}$B and $^{29}$Si projections of the $^{11}$B-$^{29}$Si correlation maps for the abovementioned glasses. As evident from the difference in intensities between the $^{11}$B (or $^{29}$Si) projections of glasses Ca-0 and Ca-15, the degree of B/Si mixing is lower in glass Ca-15 compared to glass Ca-0. A similar trend can be observed in the NC-*x* series, where the intensity of $^{11}$B (or $^{29}$Si) projections of glass NC-0 is slightly higher than the NC-15 sample (Table 3), suggesting a slightly lower B/Si mixing in the latter. However, when comparing the two series of glasses, the difference between the B/Si degree of mixing in the NC-*x* glasses is significantly smaller than in the Ca-*x* glasses. Another interesting point to note here is the decrease in the fraction/contribution of $BO_4$ units with increasing CaO/$Na_2O$ in NC-*x* glasses (in agreement with $^{11}$B MAS NMR spectra; Fig. 2b) and the corresponding change in the shape of the $^{29}$Si projections (NC-0 vs. NC-15). The difference in the shapes of $^{29}$Si projections of NC-0 and NC-15 glasses can be attributed to the changing borate speciation resulting in different types of $Q^n_{mB}$ units involved in the B/Si mixing, where *n* represents the number of bridging oxygens associated with Si and *m* is the number of $BO_3$ or $BO_4$ units in the next-nearest sphere.

*4.1.2.3. Aluminum environment in the glasses.* The $^{27}$Al MAS NMR spectra of the investigated glasses (Ca-*x* and NC-*x*; Fig. 4a and 4b) comprise one broad, asymmetric curve centered at ~65 ppm – a characteristic resonance for Al in four coordination – along with a weak signal at ~30 ppm confirming the presence of small fraction (1 % - 4 %; Table 2) of $AlO_5$ units. The presence of $AlO_5$ species has been further confirmed by the $^{27}$Al 3QMAS NMR experiments. An example spectrum is presented in Figure S6, showing a clear signal from $AlO_5$ polyhedra. Such data provide qualitative assessment of the Al speciation in these glasses, but are inherently non-quantitative due to the different magnitudes of $C_Q$ exhibited by Al in different coordination environments. In order to more accurately quantify the amount of higher coordinated Al, $^{27}$Al MAS NMR spectra were fitted initially with only the $AlO_4$ resonance, allowing full optimization of the parameters defining the position, shape and intensity of this peak. At this point, the $AlO_4$ peak fitting parameters were fixed to their optimized values and a peak describing the $AlO_5$ groups was added for additional fitting optimization. This approach, reflecting the fact that these data are mostly defined by the $AlO_4$ peak and the associated satellite transition spinning sideband, provided robust reproductions of the experimental data and consistency with the non-zero but very weak contribution of $AlO_5$ groups in the 3QMAS NMR data. From the fitting parameters of $AlO_4$ species, i.e., $\delta_{CS}$, $C_Q$, listed in Table S9, it is evident that the $^{27}$Al MAS NMR spectra of the Ca-*x* glasses show a slight increase in the isotropic chemical shift from 65.0 ppm to 67.6 ppm while the $C_Q$ value remains in the range of 5.2 – 5.5 MHz. An increase in the deshielding of Al species possibly comes from the impact of the second nearest neighbor around the Al polyhedra. In the NC-*x* series, however, it is found that the $C_Q$ value increases significantly from 4.9 to 6.1 MHz with increasing CaO concentration, which is directly reflected by the broader spectra shown in Fig. 4b. As $C_Q$ reflects the degree of symmetry of Al polyhedra, an increase in its value indicates a more distorted Al tetrahedron due to their charge compensation by a high field strength cation, i.e., $Ca^{2+}$ (instead of $Na^+$) [63]. Due to the low concentration of $AlO_5$ species, the MAS NMR peak is masked by that of the $AlO_4$ resonance. Therefore, the parameters defining the $AlO_5$ resonance have relatively large uncertainties. and are not discussed further.

Fig. 5a presents the $^{27}$Al-$^{29}$Si 2D correlation maps of glasses Ca-0, Ca-15, NC-0, and NC-15, accompanied by the $^{27}$Al and $^{29}$Si normalized projections in the horizontal and vertical axis, respectively. Similar to the B/Si mixing, all the glasses exhibit strong correlation signals suggesting a strong interaction between the aluminate and silicate network. Further, Fig. 5b shows the non-normalized $^{27}$Al and $^{29}$Si projections of the $^{27}$Al-$^{29}$Si correlation maps for the abovementioned glasses. The $^{27}$Al (or $^{29}$Si) projections for the glasses Ca-0 and Ca-15 show a nearly identical intensity (Table 3). Further, the $^{27}$Al projection signal for glass Ca-15 is broader than Ca-0 suggesting a distorted chemical environment around Al atoms in the glass structure. On the other hand, the intensity of the $^{27}$Al (or $^{29}$Si) projection for NC-15 glass is lower than NC-0 suggesting a lower Al/Si mixing in the NC-15 glass. Similar results pertaining to a decrease in the Si–O–Al connectivity due to partial substitution of $Na_2O$ by MgO have been reported by Bradtmuller et al. [68]. Meanwhile, the $^{29}$Si projection of the NC-15 sample is broader than NC-0 suggesting that different types of $Q^n_{mAl}$ units are involved in the Al/Si mixing though the degree of mixing in this glass is lower.

*4.1.2.4. Silicate environment in the glasses.* The $^{29}$Si 1D MAS NMR spectra of the four glasses, i.e., Ca-0, Ca-15, NC-0 and NC-15, along with their respective $^{29}$Si projections of the $^{11}$B/$^{29}$Si and $^{27}$Al/$^{29}$Si 2D DHMQC maps are presented in Fig. 6. The four spectra present the signal within −80 ppm to −90 ppm chemical shift range, suggesting the presence of $Q^1_{mAl/B}$ and $Q^2_{mAl/B}$ species with no clear indication about the number of connected Al/B. As reported in Table 3, the $^{29}$Si projections of the $^{29}$Si($^{11}$B) and the $^{29}$Si($^{27}$Al) NMR signals present similar features and therefore, cannot be used to determine the number of Al and B units connected in $Q^n_{mAl/B}$ moieties. Nevertheless, the 1D $^{29}$Si MAS NMR

**Table 3**
NMR signatures of the $^{29}$Si($^{11}$B) and the $^{29}$Si($^{27}$Al) species obtained from the $^{29}$Si projections of $^{29}$Si/$^{11}$B and $^{29}$Si/$^{27}$Al D-HMQC NMR spectra.

| | $^{29}$Si($^{11}$B) projection | | | $^{29}$Si($^{27}$Al) projection | | |
|---|---|---|---|---|---|---|
| | $\delta_{CS}$ (ppm) | FWHM (ppm) | Intensity (a.u.) ×10$^9$ | $\delta_{CS}$ (ppm) | FWHM (ppm) | Intensity (a.u.) ×10$^5$ |
| Ca-0 | −86.0 | 11 | 6.78 | −85.0 | 11 | 1.52 |
| Ca-15 | −81.0 | 13 | 2.92 | −83.0 | 11 | 1.59 |
| NC-0 | −87.5 | 13 | 6.61 | −87.0 | 12 | 2.00 |
| NC-15 | −89.5 | 13 | 7.87 | −88.5 | 15 | 1.40 |

$\delta_{CS}$, FWHM, and intensity are given with errors of ±0.5 ppm, ±1 ppm and ±5 %, respectively.

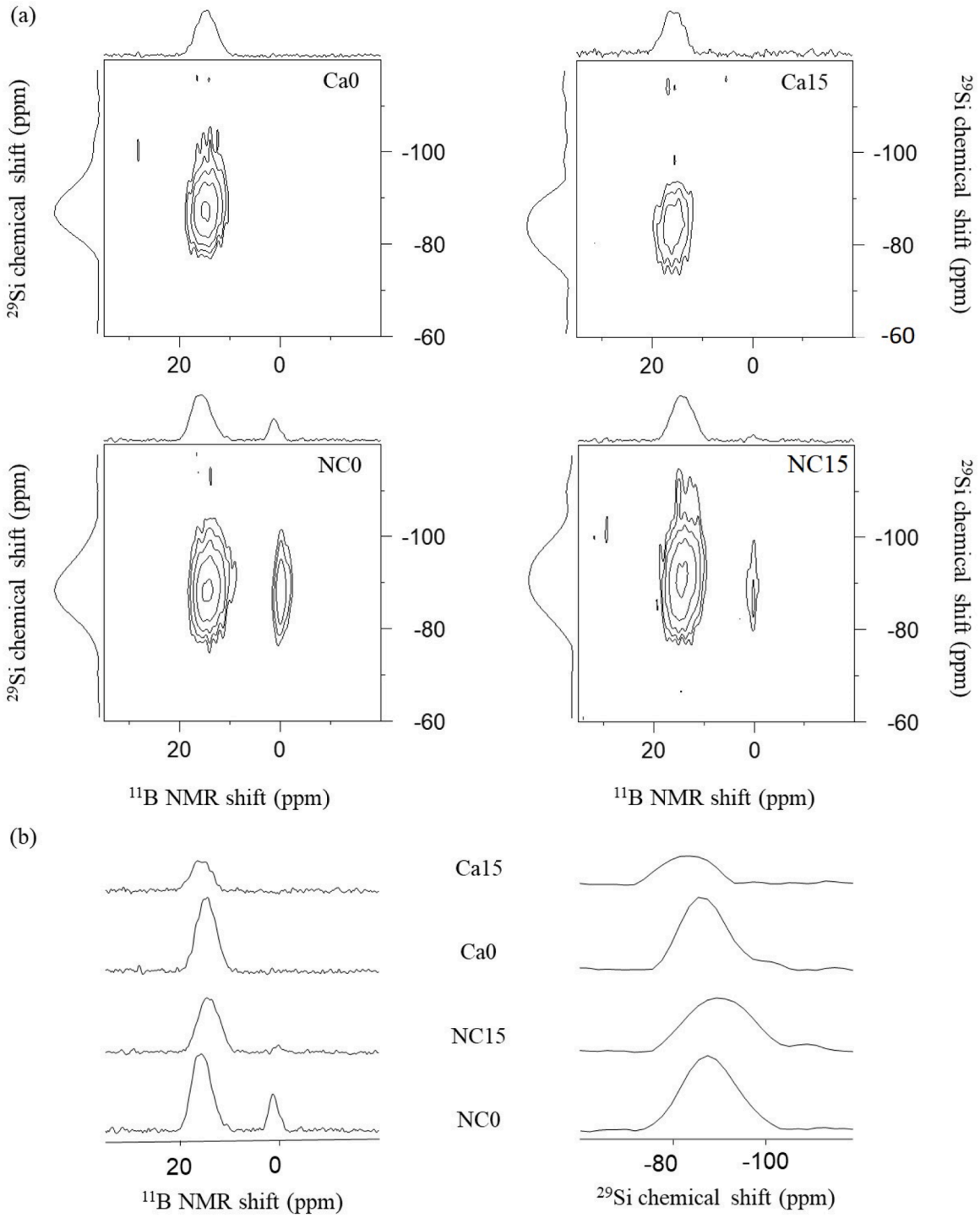


**Fig. 3.** (a) 2D $^{11}$B/$^{29}$Si maps accompanied by the $^{11}$B and $^{29}$Si projections in the horizontal and vertical axes; (b) non-normalized $^{11}$B and $^{29}$Si 2D map projections.

spectra do not show additional signals compared to the two D-HMQC projections, indicating that all the Si atoms are connected to either Al or B atoms, in good agreement with the low $SiO_2$ amounts of the compositions (that do not allow for the presence of pure $Q^4$ species ($Si(OSi)_4$).

### 4.2. Structure of glasses – MD simulations

#### 4.2.1. Reproducing glass structure by MD simulations

The MD simulations have been performed to corroborate and quantify the qualitative trends observed in the experimental investigations pertaining to the (1) $Na^+/Ca^{2+}$ environment in the glass structure and (2) degree of mixing between the network-forming moieties. In order to accomplish the abovementioned goals, the first step is to reproduce the structure of glasses in agreement with the experimental results. Accordingly, as evident from Table S10, the predicted trends pertaining to variation in boron coordination ($N_3$ and $N_4$) as a function of composition in the investigated glasses agree with the $^{11}$B MAS NMR spectroscopy results. Further, in agreement with the $^{27}$Al MAS NMR spectroscopy results, the MD simulations predict $\geq$97 % Al in the investigated glasses to be in four-coordination (Table S11). A slight mismatch between the predicted and experimental $N_3/N_4$ values or fraction of aluminum coordination may be attributed to these species'

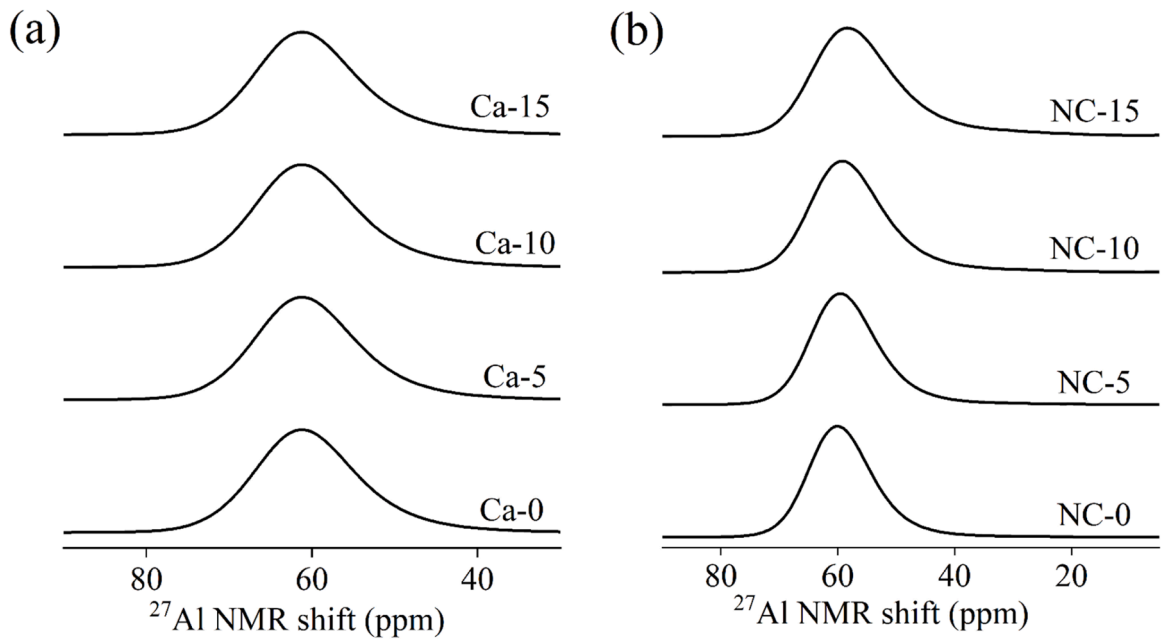


**Fig. 4.** $^{27}$Al MAS NMR spectra of (a) Ca-*x* and (b) NC-*x* series of glasses.

sensitivity to the glasses' thermal history [69,70]. Finally, the MD simulation results confirm the semi-quantitative trends for the NBO formation in the investigated glasses, as estimated using the results $^{11}$B and $^{27}$Al MAS NMR spectroscopy (Table 2). In agreement with the experimental observations, the MD simulations predict an increasing degree of depolymerization in Ca-*x* glasses, wherein 33 % - 35 % NBOs are formed in the borate network, while 60 % - 65 % NBOs in the silicate network (Table S11 and Figure S7). On the other hand, in agreement with the experimental results, varying $Na_2O/CaO$ in the NC-*x* glasses does not exhibit a considerable impact on their network connectivity (Table S11 and Figure S7). Thus, the structures reproduced by the MD simulations can be considered near-accurate representations of the experimental structure of the investigated glass compositions.

#### 4.2.2. $Na^+/Ca^{2+}$ environment in the glass structure

The results of $^{23}$Na, $^{11}$B, and $^{27}$Al MAS NMR spectroscopy suggest that $Na^+$ primarily acts as a charge-compensator for $AlO_4^-$ units in the Ca-*x* glasses, while $Ca^{2+}$ depolymerizes the glass network. Similarly, in the NC-*x* glasses, the experimental results suggest that at higher CaO concentrations, $Ca^{2+}$ replaces $Na^+$ for charge compensation of $AlO_4^-$, while there is a gradual decrease in the fraction of $BO_4$ units with increasing CaO. The MD simulations have been employed to gain further insight into the affinity of $Na^+$ and $Ca^{2+}$towards the network-forming moieties, i.e., silicate, borate, and aluminate units. Table 4 presents the relative affinities of $Ca^{2+}$ and $Na^+$ toward the network-forming moieties (labeled in their elemental forms) in the glass network, as obtained from the MD simulation results. A Ca/Na > 1 indicates the affinity of $Ca^{2+}$ towards a network forming moiety, while a Ca/Na < 1 suggests vice-a-versa. The following inferences can be drawn based on the results presented in Table 4.

1. Increasing CaO concentration in Ca-*x* glasses pushes $Na^+$ towards Al units in the glass structure, as suggested by the decreasing value of Ca/Na (for Al) from 0.977 to 0.843. This can be explained based on the constant $Na_2O/Al_2O_3$ molar ratio in all the Ca-*x* glasses and the propensity of $AlO_4^-$ to be charge-compensated by a low ionic field strength cation, i.e., $Na^+$ in this case, as discussed in Section 4.1.2.1.
2. The CaO in Ca-*x* glasses tends to distribute itself among the borate and silicate phases of the structure (creating NBOs since the majority of boron is in three-coordination – please refer to Section 4.1.2.2), as revealed by the increasing Ca/Na (for B) and Ca/Na (for Si) values for these glasses, where $Ca^{2+}$ prefers to associate with borate phase over silicate [Ca/Na (for B) > 1], thus, segregating the glass network into calcium-boron-rich and sodium-aluminosilicate-rich regions, as shown in Fig. 7. The MD simulation results are corroborated by the $^{29}$Si-$^{11}$B and $^{29}$Si-$^{27}$Al correlation NMR experiments showing a (1) decrease in Si/B mixing and (2) minimal change in the degree of Al/Si mixing, in the Ca-*x* series. A similar trend with respect to partitioning of $Ca^{2+}$ in silicate and borate phases can be expected in the NC-*x* glasses; however, on a smaller scale since a fraction of $Ca^{2+}$ is consumed for charge compensating $AlO_4^-$ units.
3. Increasing $CaO/Na_2O$ in the NC-*x* glasses results in a gradual increase in Ca/Na (for Al), thus suggesting a partial replacement of $Na^+$ by $Ca^{2+}$ as a charge-compensator of $AlO_4^-$ units, especially in glasses where $Na_2O/Al_2O_3 < 1$.

Further, the number of non-framework cations present in a network former environment have been calculated using different cutoffs taken from the end of the first peak in the Na-T and Ca-T (*T* = Si, Al, B) partial radial distribution function (Table S12). Table 4 lists the number of Na and Ca observed in the local environment of Si, Al, and B units (labeled as T-X; T: Si, Al, and B; X: Na, Ca). The values of Al-Na and Si-Na for glass Ca-0 are 4.2 and 3.6, respectively. The addition of CaO to the Ca-*x* series has a minimal impact on these values, as the values of Al-Na and Si-Na for glass Ca-15 are 3.8 and 3.5, respectively. When comparing the values of T-X from the glasses in the present investigation with those of stoichiometric pure sodium nepheline ($Na_4Al_4Si_4O_{16}$) crystal based on a fixed cutoff value of 4.0 Å or the corresponding $NaAlSiO_4$ glass with values of 3.75 and 5.2 (Fig. 8; Table S12), it is clear from the figure that the environment around silicate and aluminate tetrahedra in the Ca-*x* glasses is similar to that found in the crystalline nepheline.

On the contrary, the values of Al-Na and Si-Na in the NC-*x* glasses decreased significantly from 4.3 to 1.9 and 3.7 to 1.7, respectively, with increasing CaO content. The observed trend in NC-*x* glasses is not surprising as the concentration of $Na_2O$ is being gradually replaced by CaO, thus resulting in a concomitant increase in the values of Al-Ca and Si-Ca. Therefore, the environment around the aluminosilicate network in the NC-*x* glasses differs considerably from that observed in a nepheline crystal. Finally, the change in glass chemistry did not significantly impact the coordination number of $Na^+$ and $Ca^{2+}$, as calculated by the

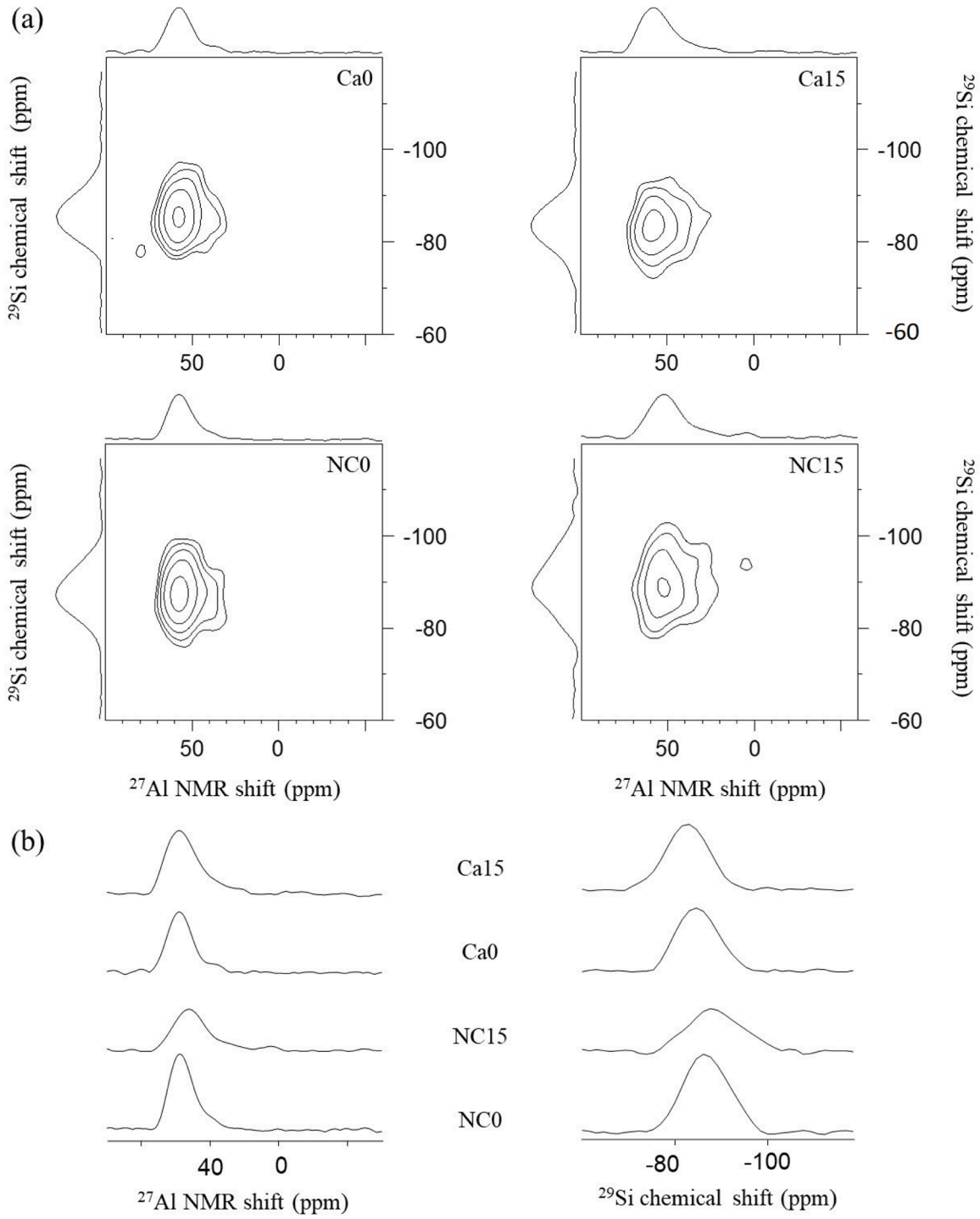


**Fig. 5.** (a) 2D $^{27}$Al/$^{29}$Si maps accompanied by the $^{27}$Al and $^{29}$Si projections in the horizontal and vertical axes, (b) Non-normalized $^{27}$Al and $^{29}$Si 2D maps projections.

MD simulations. The coordination number of the cations varies between 5 and 6 in the investigated glasses (Table 4).

### 4.3. Crystallization in glass melts

Table S13 presents the liquidus temperature ($T_L$) of the investigated glasses. Here it must be mentioned that we could not measure the $T_L$ for glasses NC-10 and NC-15 due to their minimal tendency toward crystallization. In general, the $T_L$ decreases with increasing CaO in both the series of glasses, with nepheline ($NaAlSiO_4$; PDF # 98–000–0327) being the first phase to crystallize at the $T_L$.

Fig. 9 presents the quantitative phase analysis of the CCC-treated glasses. In the Ca-*x* series, the propensity of crystallization increases with the addition of CaO, wherein nepheline dominates the phase assemblage. For example, the phase assemblage of CCC-treated glass Ca-0 comprises 24 wt.% nepheline (PDF # 98–000–0327) and 76 % residual glassy phase. However, the addition of CaO increased the (weight) fraction of nepheline to 70 %−80 % along with the crystallization of small fractions (7 %−14 %) of calcium borate-based phases, for example, $Na_{0.64}Ca_{0.69}Al_2B_2O_7$ (PDF #04–011–7558), $Ca(BO_3)_2$ (PDF #04–015–4245) and $Ca_2B_2O_5$ (PDF #04–009–3864). These results are intriguing as borate-based phases generally exhibit a low tendency

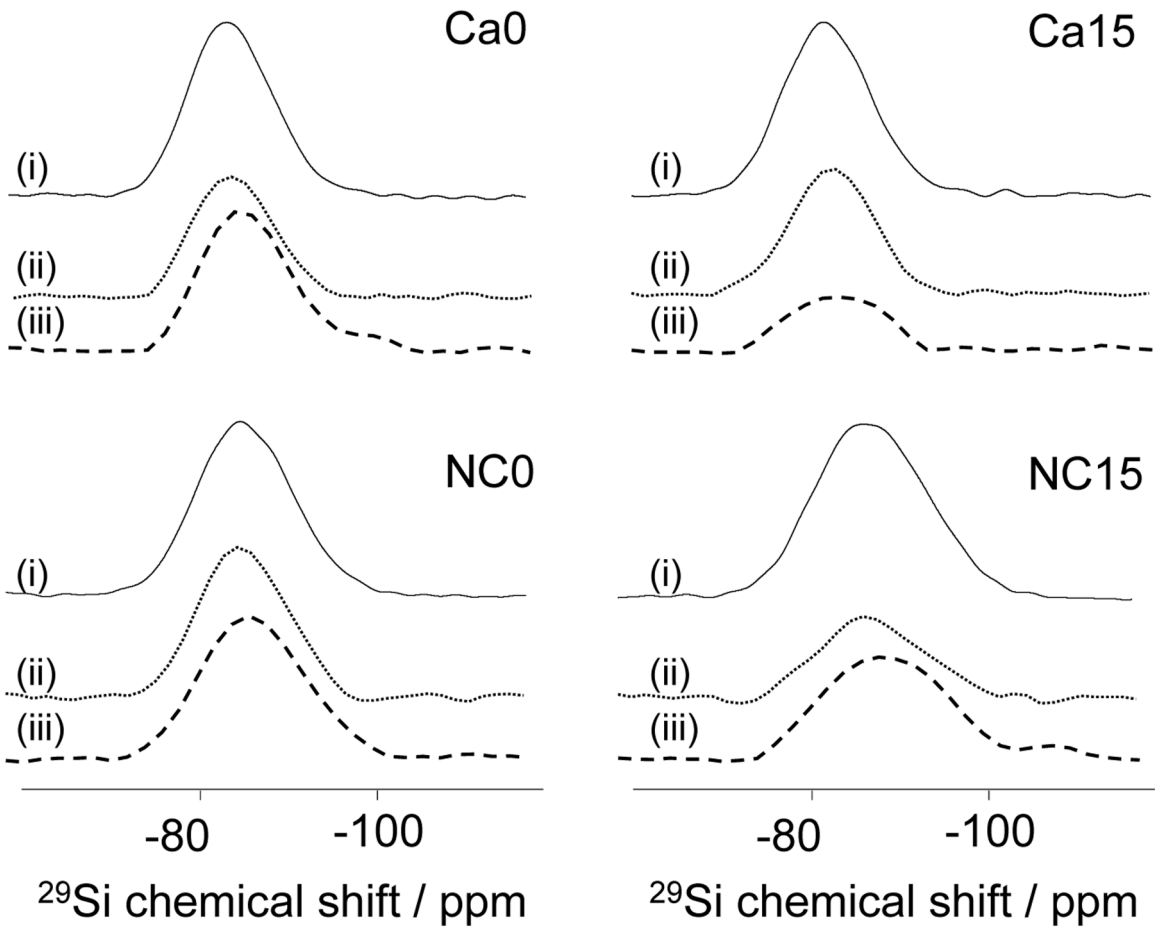


**Fig. 6.** Comparison between the $^{29}$Si MAS-NMR (i) and the $^{29}$Si projections of the $^{11}$B/$^{29}$Si (ii) and $^{27}$Al/$^{29}$Si (iii) 2D DHMQC maps.

**Table 4**
Relative affinity of $Ca^{2+}$ and $Na^{+}$ (Ca/Na) to network formers, number of Na/Ca found in the local environment of Si, B and Al, and the average coordination number of Na and Ca in the glass network.

| | Relative affinity Ca/Na | | | Number of Na/Ca in the local environment of Si, B and Al [a] | | | | | | Average coordination number | |
|---|---|---|---|---|---|---|---|---|---|---|---|
| | Al | B | Si | Al-Na | Si-Na | B-Na | Al-Ca | Si-Ca | B-Ca | Na | Ca |
| Ca-0 | / | / | / | 4.218 | 3.674 | 3.535 | / | / | / | 5.53 | / |
| Ca-5 | 0.977 | 1.159 | 0.942 | 4.044 | 3.682 | 3.498 | 0.402 | 0.391 | 0.426 | 5.61 | 5.66 |
| Ca-10 | 0.875 | 1.231 | 0.997 | 3.954 | 3.626 | 3.318 | 0.752 | 0.858 | 0.907 | 5.67 | 5.77 |
| Ca-15 | 0.843 | 1.200 | 1.012 | 3.837 | 3.551 | 3.321 | 1.104 | 1.348 | 1.402 | 5.74 | 5.81 |
| NC-0 | / | / | / | 4.300 | 3.749 | 3.749 | / | / | / | 5.62 | / |
| NC-5 | 0.949 | 1.161 | 0.955 | 3.558 | 3.108 | 2.992 | 0.384 | 0.371 | 0.434 | 5.67 | 5.67 |
| NC-10 | 0.969 | 1.182 | 0.958 | 2.763 | 2.418 | 2.218 | 0.786 | 0.806 | 0.872 | 5.73 | 5.94 |
| NC-15 | 1.004 | 1.216 | 0.995 | 1.895 | 1.660 | 1.423 | 1.264 | 1.227 | 1.327 | 5.81 | 5.98 |

[a] The values of Na around Al and Si units (which are identical) in pure nepheline crystal are calculated to be 3.75 with a fixed cutoff distance of 4.0 Å, and 5.2 with the same cutoff values used in the calculation of the glasses. The cutoff values used can be found in Table S9.

towards crystallization in alkali aluminoborosilicate borosilicate glasses, as observed in our previous study [48]. Nonetheless, the high propensity of nepheline precipitation and crystallization of calcium borate phases correlate well with the following structural trends observed in these glasses: (1) the addition of CaO to the Ca-*x* glasses pushes $Na^{+}$ closer to $AlO_4$ units in the glass structure, while $Ca^{2+}$ prefers to associate with borate phase (from MAS NMR and MD simulations), and (2) the addition of CaO promotes de-mixing between borate and silicate units in the Ca-*x* glasses, while the mixing between aluminate and silicate units increases or remains identical (from $^{29}$Si-$^{27}$Al D-HMQC NMR spectroscopy); (3) the environment of aluminosilicate network in the Ca-*x* glasses is similar to that observed in a nepheline crystal (from MD simulations). Considering the abovementioned structural details, it is not surprising that the Ca-*x* glasses exhibit a high tendency towards nepheline crystallization along with several types of calcium borate phases (depending on CaO concentration in glass).

When discussing the crystallization behavior of CCC-treated NC-*x* glasses, the glass NC-0 exhibits a high propensity to crystallize nepheline (56 wt.%)—however, the substitution of 5 mol.% CaO for $Na_2O$ in the glass NC-5 almost completely suppresses the crystallization resulting in a 99 % amorphous sample. Further, an increase in CaO concentration to ≥10 mol.% results in a 100 % amorphous sample upon CCC-treatment. The results are, once again, intriguing as according to the $NaAlSiO_4$ – $CaAl_2Si_2O_8$ phase diagram [71] and based on the crystallization behavior of glass NC-0, one should expect the crystallization of a mixture of anorthite ($CaAl_2Si_2O_8$) and nepheline/carnegiete (a polymorph of $NaAlSiO_4$) based phases or a $Na_{(2-x)}Ca_xAl_2Si_2O_8$ solid solution, as has been shown in our previous study [30]. However, the near-complete

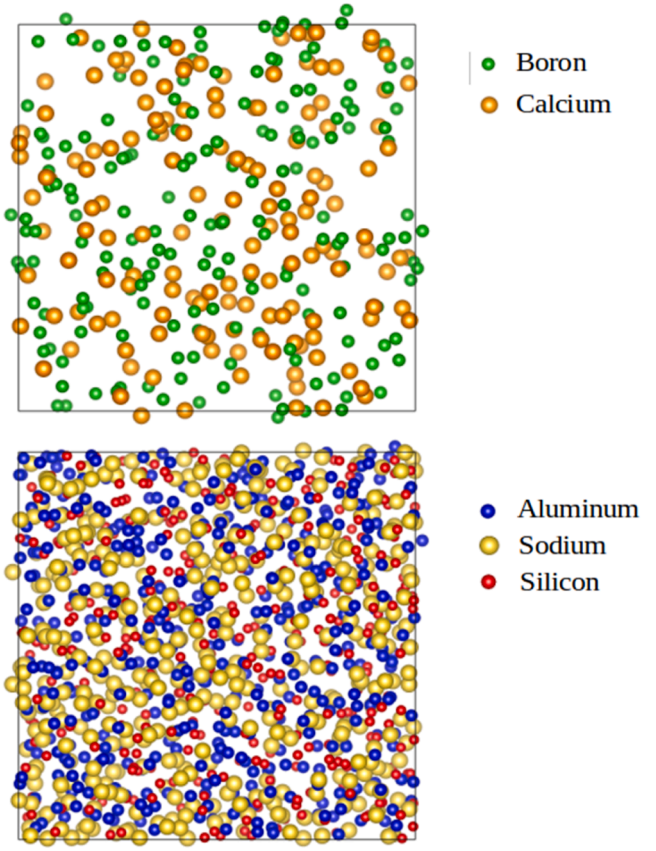


**Fig. 7.** Snapshot of the MD structure of Ca-15 glass showing the aggregation of Ca and B atoms (upper panel) and Na, Al and Si atoms (lower panel).

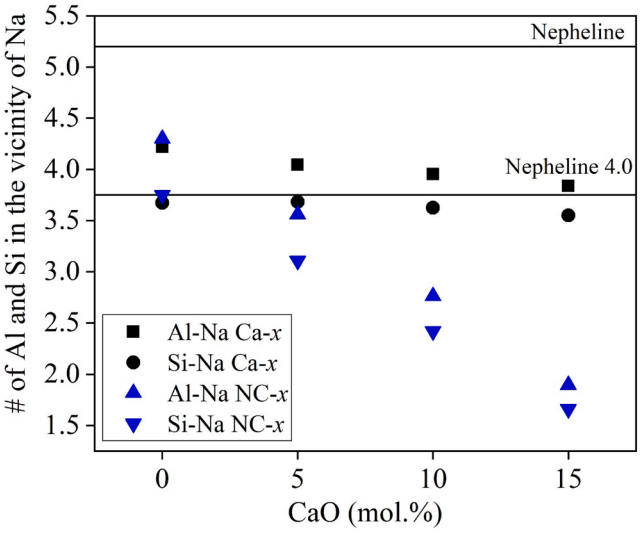


**Fig. 8.** The values of Na around Al and Si units in the investigated glass (presented as symbols) and synthetic nepheline (presented as a solid lines). The line labeled as 'Nepheline' represents the value calculated using the same cut-off radius as those used in glass and the line labeled as 'Nepheline 4.0′ represents the value calculated using a fixed cut-off radius of 4.0 Å. (Note: Al-Na and Si-Na numbers are identical in crystalline nepheline, thus represented as one single line).

suppression of crystallization by substitution of only 5 mol.% $Na_2O$ by CaO is interesting and warrants further discussion. A review of the structural trends observed in NC-*x* glasses brings the following details to the forefront:

1. Since $Ca^{2+}$ is substituting an equimolar concentration of $Na^+$, the $AlO_4^-$ units are increasingly charge-compensated by $Ca^{2+}$ due to insufficient $Na^+$ in the glass network. Therefore, the amount of $Ca^{2+}$ partitioning to the borate network is smaller than that in the Ca-*x* series. This is also evident from the trends observed for NBO fraction in the investigated glasses (from Raman and MAS NMR spectroscopy). Thus, the chemical and structural environment required for the nucleation and crystallization of calcium borate phases could not be formed in the NC-*x* series.
2. An increase in $CaO/Na_2O$ in the NC-*x* glasses results in a decreased Al/Si mixing, i.e., lower Si–O–Al connectivity (from D-HMQC spectroscopy). Further, there is a significant change in the environment of the aluminosilicate network with an increase in $CaO/Na_2O$, as the concentration of $Na^+$ in the aluminosilicate environment decreases, while that of $Ca^{2+}$ increases (from MD simulations). Our previous studies show that nepheline crystallization requires a higher fraction of Si–O–Al linkages, where $AlO_4^-$ units are being charge-compensated by $Na^+$. These conditions are not fulfilled in the NC-*x* glasses due to a decrease in Al/Si mixing, and the decreasing concentration of $Na^+$ from the aluminosilicate network. Further, suppressing crystallization of the anorthite ($CaAl_2Si_2O_8$) phase in CaO-rich glasses helps extend (and strengthen) the hypothesis that it is primarily the Si/Al mixing in the glass network that is the governing descriptor controlling the crystallization of an aluminosilicate phase in the aluminoborosilicate glasses.

### *4.4. MD simulations-based model to predict the crystallization behavior and propensity of the investigated glasses*

Based on the composition – structure – crystallization behavior relationships observed in the investigated glasses, a cluster analysis model (powered by MD simulations) [72] has been developed to predict the behavior and propensity of crystallization in the alkali aluminoborosilicate glasses. The model assumes that the nucleation and growth of crystalline phases in a multicomponent oxide glass is facilitated by clusters of atoms (known as 'embryos') in the glass structure, with their stoichiometry and structure similar to that of the crystal phase. The cluster analysis explores simulated structures quantifying the similarity between the atomic environments in glass and the reference crystal. Atomic aggregates (clusters) within a pre-defined cut-off from the central atom in the glass model are compared with the ones of a reference crystalline structure, providing a cumulative displacement between the radial distribution function up to the pre-defined cut-off. An in-depth description of the cluster analysis and its algorithm has been reported elsewhere [7].

In the present investigation, we focused on the local environment of oxygen atoms within a cutoff of 7 Å, which can be compared with the six different oxygens in synthetic nepheline. The minimum cumulative displacement (MCD) averaged among the six oxygens sites in nepheline crystal has been computed and used as a guideline to estimate the possible crystallization of the nepheline phase in the glass, as shown in Table S14 and Fig. 10. The cut-off was chosen to seek embryos of dimension comparable to 2–3-unit cells.

As evident from Table S14 and Fig. 10, all the glasses in the Ca-*x* and NC-*x* series, in which the nepheline phase crystallizes upon CCC treatment, show an average MCD lower than 102. Further, when extended to the glasses in the $Na_2O$-$Al_2O_3$-$B_2O_3$-$SiO_2$ and $Li_2O$—$Na_2O$-$Al_2O_3$-$B_2O_3$-$SiO_2$ systems investigated in our previous studies (Fig. 10) [25], the cluster model correctly predicted their propensity toward nepheline crystallization, where the OB and sub-mixture models had failed (except for glass BL-2, which showed ~3 vol.% nepheline crystallization upon

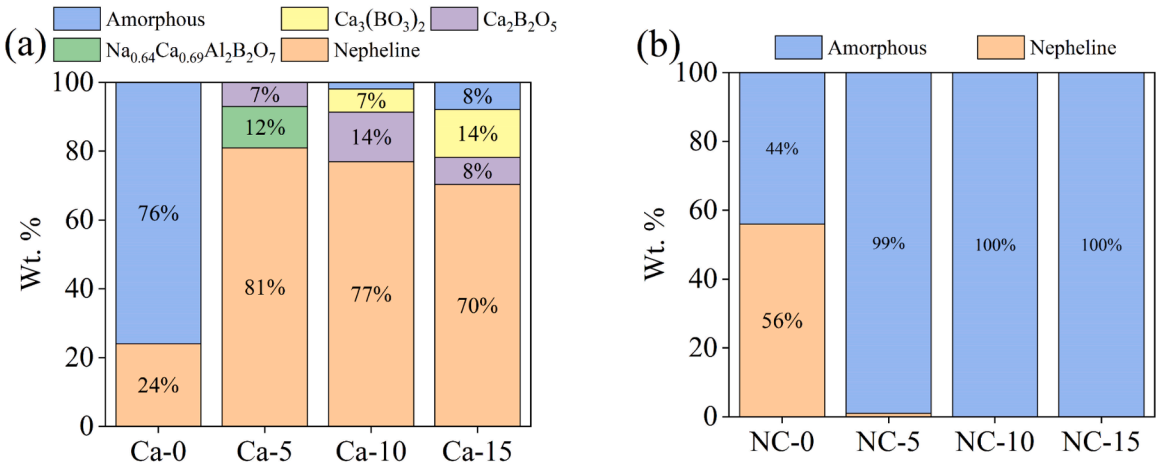


**Fig. 9.** Quantitative phase analysis of the CCC-treated glasses of (a) Ca-*x* series and (b) NC-*x* series. (Standard deviation: ± 1 wt%).

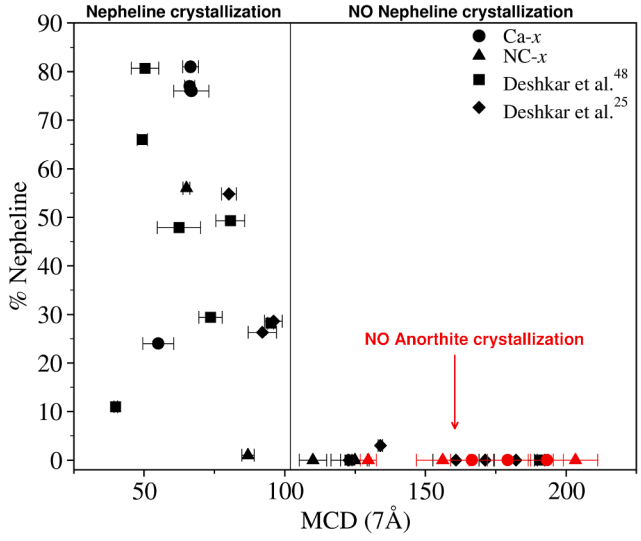


**Fig. 10.** Percentage of nepheline crystallization as a function of the Minimum Cumulative Displacement (MCD) within a cutoff of 7 Å in the glasses investigated in the present study and from Deshkar et al.[48] The red symbols indicate MCD values for anorthite crystal in Ca-containing glasses. The black line represents the threshold for crystallization.

CCC treatment). The batched compositions (in wt.%), OB values, and nepheline crystallization propensity predicted by sub-mixture model of selective glasses from Deshkar et al. [48] are presented in Table S15.

To better validate the model, the MCD value of anorthite ($CaAl_2Si_2O_8$) crystal, an isochemical analogue of nepheline ($Na_2Al_2Si_2O_8$) where $Na_2O$ has been replaced by CaO, was computed and compared with the MCD value of nepheline. The MCD for anorthite in all the CaO containing glasses in the NC-*x* and Ca-*x* series is significantly higher than 102 (Fig. 10 and Table S14), i.e., the threshold for the crystallization of nepheline-like phases, thus, predicting minimal chance for its crystallization even in glasses with highest concentration of CaO and confirming the prowess of the model.

It is worth mentioning that the present model has been calibrated for the prediction of nepheline crystallization in the $Li_2O$—$Na_2O$—CaO-$Al_2O_3$-$B_2O_3$-$SiO_2$ systems. Our future studies will focus on enlarging the dataset to predict crystallization tendency of glasses designed in other compositional domains. The overarching goal is to develop a rigorous QSPR-based model that can make high fidelity predictions about the crystallization tendency of glasses over a broad compositional space.

## 5. Discussion

### 5.1. Implications of the study on our understanding of the structure of alkali aluminoborosilicate glasses

$Ca^{2+}$, owing to its high ionic field strength (0.33 $Å^{-2}$), is known to induce tangible changes in the short–to–intermediate/medium range ordering in the structure of alkali aluminoborosilicate glasses. For example, it (1) promotes the formation of $BO_3$ units at the expense of $BO_4$ along with the formation of NBOs, as shown in Eq. (4) [53,63,73]; (2) promotes the formation of five-coordinated aluminum units [30,74]; and (3) may induce heterogeneity/phase separation [63]. Here, it needs to be mentioned that although $Ca^{2+}$ (and other high ionic field strength cations, e.g., $La^{3+}$, $Zr^{4+}$, $Nb^{5+}$) are known to promote the formation of $BO_3$ units at the expense of $BO_4$ units, majority of these glasses have low R (= $Na_2O_{excess}/B_2O_3$) values, i.e., $R < 0.7$, where $[Na_2O_{excess}] = [Na_2O] - [Al_2O_3]$ [75]. In the present study, the R-value of glass NC-0 is 0.6. At higher R values, i.e., ≥0.7, an opposite trend for $BO_3/BO_4$ formation has been reported in binary alkali/alkaline-earth borate glasses, where the $BO_4$ fraction in $Na_2O$-$B_2O_3$ glass is lower than the corresponding CaO-$B_2O_3$ glass [76]. Since borosilicate glasses are generally considered dilute borates [77], a similar trend may also manifest in the borosilicate and aluminoborosilicate glasses.

Further, suppose we generalize $Ca^{2+}$ as a high-field strength alkali/alkaline-earth non-framework cation, for example, $Li^+$ or $Mg^{2+}$. In that case, we can expect de-mixing of Al/Si and B/Si network, as has been shown by Bradtmuller et al. [68] and Bisbrouck et al. [78,79] in sodium-magnesium aluminoborosilicate glasses, and by Du and Stebbins in lithium borosilicate [80] and lithium-sodium borosilicate glasses [81]. Here, it needs to be emphasized that in most of the studies discussed in the literature, the high-field strength alkali/alkaline-earth cation (e.g., $Li^+$, $Mg^{2+}$, $Ca^{2+}$) has been substituted (or wholly replaced) for a low-field strength alkali/alkaline-earth cation, for example, $Na^+$, $K^+$, $Ba^{2+}$.

In the present study, $Ca^{2+}$ has been introduced into the glass system via two different approaches. In the first approach, CaO was added to the glass composition while maintaining the overall molar ratios of all the glass constituents to be constant, i.e., Ca-*x* glasses. In the second approach, CaO has been gradually substituted for $Na_2O$ in the system, thus decreasing the Na/Al in the glass structure (NC-*x* glasses). The structural trends observed in the NC-*x* glasses align with the literature, where one observes a gradual decrease in $N_4$ fraction and chemical heterogeneity (in terms of mixing different network former moieties) with increasing $CaO/Na_2O$.

On the contrary, the structural trends observed in Ca-*x* glasses are intriguing and not reported in the literature. If we generalize $Ca^{2+}$ as a

high field strength cation (in league with $La^{3+}$, $Zr^{4+}$, $Nb^{5+}$, etc.), one should expect a decrease in $N_4$ fraction with the addition of CaO to the glasses in Ca-*x* series, as has been reported by Qin et al. [75] In the present study, the glass Ca-0 is metaluminous [(Na+Ca)/Al =1] in nature. Therefore, we do not expect any $BO_4$ units in the glass structure as $Na^+$ is entirely consumed by charge compensating the $AlO_4$ units. Although the addition of CaO to the Ca-*x* glasses shifts them from metaluminous to peralkaline [(Na+Ca)/Al >1] regime, the $N_4$ fraction is still minimum. Such an observation further suggests that $Ca^{2+}$, due to its high field strength, exhibits a high preference for negatively charged NBOs to stabilize its coordination instead of facilitating the $BO_3 \rightarrow BO_4$ conversion.

Further, in terms of mixing/de-mixing of network-forming moieties with the introduction of $Ca^{2+}$ to the investigated glass systems, though it is challenging to zero down on the exact reason for the trends observed in D-HMQC NMR studies, based on the results of 1D MAS NMR spectroscopy, MD simulations, and literature [81–83], it can be hypothesized that the following structural descriptors play an essential role in dictating the observed trends: (1) Na/Al and R; (2) the ionic field strength of $Ca^{2+}$; (3) which cation – $Na^+$ or $Ca^{2+}$ – is charge-compensating $AlO_4^-$ units. The abovementioned structural descriptors will be instrumental in deciding the (1) short-range ordering in the glass structure, i.e., silicate, borate, and aluminate speciation, (2) concentration and stabilization of Al–O–Al linkages [68], (3) concentration of ring/non-ring $BO_3$ units and their connectivity with $SiO_4$ or $BO_4$ units [75], and (4) chemical environment around the aluminosilicate network, thus, defining the mixing/de-mixing of network forming units in the glass structure.

### 5.2. Deciphering the structural descriptors controlling crystallization in aluminoborosilicate glasses

It has been well-established that ordering at short-length and, in some cases, at intermediate-length scales is a universal feature of the glassy state [3,84-86]. According to Zanotto and Cassar [3], the poor nucleation in albite ($NaAlSi_3O_8$) glass is due to the significant differences in the atomic structure of the parent melt vis-à-vis its isochemical crystalline phase. However, extending this hypothesis to multicomponent glasses is challenging due to their compositional and structural complexity.

In the past few years, we have worked towards deciphering the structural descriptors governing the crystallization of alkali aluminoborosilicate based glasses designed in the primary crystallization field of nepheline. The focus of our previous studies was on understanding the interaction between network formers (e.g., $SiO_2/B_2O_3$, $Al_2O_3/B_2O_3$, $SiO_2/P_2O_5$, $Al_2O_3/P_2O_5$, $B_2O_3/P_2O_5$, and $Al_2O_3/Fe_2O_3$) and their impact on the propensity of crystallization in glasses of the sodium aluminoborosilicate family [29,48,87,88]. These studies clearly show that the higher degree of mixing between the $SiO_4$ and $AlO_4$ units, i.e., Si–O–Al linkages, in the glass structure promotes the crystallization of aluminosilicate phases. Outcomes of these studies have led to a hypothesis: if these Si–O–Al linkages are broken or replaced, for example by Si–O–B or Al–O–P linkages, it will be difficult for nucleation and growth of crystalline aluminosilicate phases to occur. The present study aims to (1) test the validity of this hypothesis in glass systems with more than one non-framework cations, i.e., $Na^+$ and $Ca^{2+}$, while maintaining constant molar ratios of network forming units and (2) unearth additional structural descriptors, if any, through which a non-framework cation, for example, $Ca^{2+}$, may influence the tendency of glass to crystallize. While the results from the present investigation confirm the validity of the above-discussed hypothesis, they also elucidate the difference/similarity between the short-to-intermediate range ordering in the glass structure to that of the structure of corresponding crystalline phase (being controlled by the roles of $Na^+$ and $Ca^{2+}$ in the glass structure) as another key descriptor governing the nucleation of an aluminosilicate phase.

Future studies on this subject will be focused on understanding the impact of low ionic field strength cations, for example, $K^+$ and $Ba^{2+}$, on the structure and crystallization behavior of sodium aluminoborosilicate glasses with OB $\leq$ 0.57. The low ionic field strength cations are expected to exhibit random mixing in the glass structure, thereby affecting the driving force for nucleation and growth of crystalline phases [53,54,89]. Therefore, studying the chemo-structural descriptors controlling crystallization in these glasses will be interesting.

### 5.3. Implications on the development of quantitative structure-property relationship (QSPR) models for predicting crystallization behavior of aluminoborosilicate glasses

Among all the predictive models discussed in Section 2.2, the OB model has been able to correctly predict the crystallization tendency of all the glasses in the present study. Thus, the conservative nature and incorrect predictions of the ND and sub-mixture models are evident from the results presented in this study. With that said, it is worth noting that although the OB model has successfully predicted the likelihood of crystallization of glasses in the present study, it has failed to do so in our previous studies [25,26]. This warrants the transition from empirical models towards QSPR models, wherein MD simulations and experimental datasets can be combined and processed using machine learning frameworks to develop theory-guided, data-driven predictive models that can reliably predict the crystallization behavior of multicomponent glasses (e.g., comprising low ionic field strength cations, as discussed in Section 5.2) based on their chemo-structural descriptors. As an example, the proposed cluster model (powered by MD simulations) could be an effective tool for estimating the rate and degree of nepheline crystallization in multicomponent glasses. A similar approach, employing machine learning models to establish correlations between the structure and crystallization tendency (and pathway) in soft colloidal glasses, was proposed in a recent study [90]. The present study is a pioneering step towards establishing similar relationships in multicomponent oxide glasses, wherein the strengths of experimental materials science have been combined with MD simulations to establish the connections between their structure and crystallization behavior; fundamental understanding of these connections is key to the development of a QSPR-based predictive model. However, it is important to highlight that the reliability of the MD simulations is affected by the (1) accuracy of the interatomic potential used, (2) cooling rate, which is several orders of magnitude faster than those employed in experiments, and (3) dimension of the computational volume, which should be large enough to avoid correlation effects and to show heterogeneous structures with formation of regions richer in particular ions. Accelerated MD simulations exploiting accurate interatomic potentials derived from machine learning models [91–95], coupled with enhanced sampling techniques [96] could be used to produce reliable glass structures and for studying the evolution of crystallization process, as recently done for simple stoichiometric systems [6,7,97,98].

## 6. Conclusion

An attempt has been made to combine experimental and computational materials science to unearth the chemo-structural descriptors governing the propensity of crystallization in the alkali/alkaline-earth aluminoborosilicate glasses designed in the primary phase field of nepheline, $NaAlSiO_4$. Two series of glasses (Ca-*x* and NC-*x*) in the system $Na_2O$—CaO-$Al_2O_3$-$B_2O_3$-$SiO_2$ have been designed based on the predictions of optical basicity (OB) model pertaining to the nepheline crystallization in the investigated glasses upon cooling from the melt stage. i.e., OB < 0.55–0.57 – suppression of nepheline crystallization, where OB (Ca-*x*) > 0.57 and OB (NC-*x*) $\leq$ 0.57. The experimental results concerning the propensity of crystallization in the investigated glasses align with the predictions of the OB model, but not with those of sub-mixture model. The results from experimental and computational

studies reveal the following two descriptors that govern the nucleation and crystallization of a particular aluminosilicate phase in the functional glasses: (1) degree of mixing between the $SiO_4$ and $AlO_4$ units, i.e., Si–O–Al linkages, and (2) difference/similarity between the short-to-intermediate range ordering in the glass structure to that of the structure of corresponding crystalline phase. Based on the established composition – structure – crystallization behavior relationships, a cluster analysis based QSPR model has been developed to predict the propensity of the investigated glasses towards nepheline (and anorthite) crystallization. The model has been tested on a limited number of compositions from the present and previous studies [25,48] and has successfully predicted the crystallization propensity of all the glass compositions, especially for those compositions where the ND, OB and/or sub-mixture models failed.

## Declaration of competing interest

The authors declare that they have no known competing financial interests or personal relationships that could have appeared to influence the work reported in this paper.

## Acknowledgment

This material is based upon work supported by funding provided by the US Department of Energy (DOE), Office of River Protection, Waste Treatment & Immobilization Plant (WTP), through contract numbers 89304018CEM000006 and 89304022CEM000015, and the National Science Foundation under Grant No. 2034871.

## Supplementary materials

Supplementary material associated with this article can be found, in the online version, at doi:10.1016/j.actamat.2024.119784.

## References

[1] D. Turnbull, Under what conditions can a glass be formed? Contemp. Phys. 10 (5) (1969) 473–488.
[2] J. Jiusti, E.D. Zanotto, D.R. Cassar, M.R.B. Andreeta, Viscosity and liquidus-based predictor of glass-forming ability of oxide glasses, J. Am. Ceram. Soc. 103 (2) (2020) 921–932.
[3] E.D. Zanotto, D.R. Cassar, The microscopic origin of the extreme glass-forming ability of Albite and B 2 O 3, Sci. Rep. 7 (1) (2017) 1–13.
[4] M.E. McKenzie, B. Deng, D.C. Van Hoesen, X. Xia, D.E. Baker, A. Rezikyan, R. E. Youngman, K.F. Kelton, Nucleation pathways in barium silicate glasses, Sci. Rep. 11 (1) (2021) 69.
[5] C.J. Wilkinson, D.R. Cassar, A.V. DeCeanne, K.A. Kirchner, M.E. McKenzie, E. D. Zanotto, J.C. Mauro, Energy landscape modeling of crystal nucleation, Acta Mater. 217 (2021) 117163.
[6] F. Lodesani, M.C. Menziani, S. Urata, A. Pedone, Evidence of multiple crystallization pathways in lithium disilicate: a metadynamics investigation, J. Phys. Chem. Lett. 14 (2023) 1411–1417.
[7] F. Lodesani, M.C. Menziani, K. Maeda, Y. Takato, S. Urata, A. Pedone, Disclosing crystal nucleation mechanism in lithium disilicate glass through molecular dynamics simulations and free-energy calculations, Sci. Rep. 10 (1) (2020) 17867.
[8] A. Tandia, M.C. Onbasli, J.C. Mauro, Machine Learning for Glass Modeling, in: J.D. Musgraves, J. Hu, L. Calvez (Eds.), Springer Handbook of Glass, Springer International Publishing, Cham, 2019, pp. 1157–1192.
[9] J.C. Mauro, A. Tandia, K.D. Vargheese, Y.H.Z. Mauro, M.M. Smedskjaer, Accelerating the design of functional glasses through modeling, Chem. Mater. 28 (12) (2016) 4267–4277.
[10] X. Xu, T. Han, J. Huang, A.A. Kruger, A. Kumar, A. Goel, Machine learning enabled models to predict sulfur solubility in nuclear waste glasses, ACS Appl. Mater. Interfaces 13 (2021) 53375–53387.
[11] I. Sargin, C.E. Lonergan, J.D. Vienna, J.S. McCloy, S.P. Beckman, A data-driven approach for predicting nepheline crystallization in high-level waste glasses, J. Am. Ceram. Soc. 103 (9) (2020) 4913–4924.
[12] X. Lu, I. Sargin, J.D. Vienna, Predicting nepheline precipitation in waste glasses using ternary submixture model and machine learning, J. Am. Ceram. Soc. 104 (2021) 5636–5647.
[13] A. Goel, J.S. McCloy, R. Pokorny, A.A. Kruger, Challenges with vitrification of Hanford High-Level Waste (HLW) to borosilicate glass – an overview, J. Non-Cryst. Solids: X 4 (2019) 100033.
[14] W. Holand, G.H. Beall, Composition Systems for Glass-Ceramics, Glas-Ceramic Technology, John Wiley & Sons, Inc., Hoboken, NJ, 2012.
[15] D.A. Duke, J.F. MacDowell, B.R. Karstetter, Crystallization and chemical strengthening of nepheline glass-ceramics, J. Am. Ceram. Soc. 50 (2) (1967) 67–74.
[16] E.M.A. Hamzawy, E.A.M. El-Meliegy, Preparation of nepheline glass–ceramics for dental applications, Mater. Chem. Phys. 112 (2) (2008) 432–435.
[17] J.F. MacDowell, Microwave heating of nepheline glass-ceramics, Am. Ceram. Soc. Bull. 63 (2) (1984) 282.
[18] J.F. MacDowell, Microwave-compatible nepheline glass-ceramics, US Patent (1982) 4341872.
[19] M.C. Wang, N.C. Wu, M.H. Hon, Preparation of nepheline glass-ceramics and their application as dental porcelain, Mater. Chem. Phys. 37 (4) (1994) 370–375.
[20] J. Li, M. Wang, P. Lu, Nucleating role of $P_2O_5$ in nepheline-based transparent glass-ceramics, J. Am. Ceram. Soc. 104 (11) (2021) 5614–5624.
[21] A.J. Ellison, L.A. Moore, T.L. Werner, Opaque colored glass-ceramics comprising nepheline crystal phases, US Patent 9718725B2 (2016).
[22] M.J. Dejneka, A.J. Ellison, J.C. Mauro, Ion exchangeable glass with high damage resistance, US Patent 9517967B2 (2016).
[23] M.J. Dejneka, A.J. Ellison, J.C. Mauro, Zircon compatible, ion exchangeable glass with high damage resistance, US Patent 11447415B2 (2013).
[24] J.S. McCloy, M.J. Schweiger, C.P. Rodriguez, J.D. Vienna, Nepheline crystallization in nuclear waste glasses: progress toward acceptance of high-alumina formulations, Int. J. Appl. Glass Sci. 2 (3) (2011) 201–214.
[25] A. Deshkar, B. Parruzot, R.E. Youngman, O. Gulbiten, J.D. Vienna, A. Goel, Compositional dependence of crystallization and chemical durability in alkali aluminoborosilicate glasses, J. Non-Cryst. Solids 590 (2022) 121694.
[26] A. Goel, J.S. McCloy, K.M. Fox, C.J. Leslie, B.J. Riley, C.P. Rodriguez, M. J. Schweiger, Structural analysis of some sodium and alumina rich high-level nuclear waste glasses, J. Non-Cryst. Solids 358 (3) (2012) 674–679.
[27] H. Li, J. Vienna, P. Hrma, D. Smith, M. Schweiger, Nepheline precipitation in high-level waste glasses: compositional effects and impact on the waste form acceptability, MRS Online Proc. Library Archive 465 (1996).
[28] J.D. Vienna, J.O. Kroll, P.R. Hrma, J.B. Lang, J.V. Crum, Submixture model to predict nepheline precipitation in waste glasses, Int. J. Appl. Glass Sci. 8 (2) (2017) 143–157.
[29] Y. Zhang, N. Balasubramanya, N. Stone-Weiss, S. Kamali-Moghaddam, R. Youngman, P. Florian, A. Goel, Insights into the iron and phosphorus induced structural rearrangements in sodium aluminoborosilicate glasses and its impact on their melt rheology and crystallization behavior, J. Phys. Chem. C 126 (51) (2022) 21771–21792.
[30] A. Deshkar, J. Marcial, S.A. Southern, L. Kobera, D.L. Bryce, J.S. McCloy, A. Goel, Understanding the structural origin of crystalline phase transformations in nepheline ($NaAlSiO_4$) based glass-ceramics, J. Am. Ceram. Soc. 100 (7) (2017) 2859–2878.
[31] D.R. Neuville, B.O. Mysen, Role of aluminium in the silicate network: in situ, high-temperature study of glasses and melts on the join $SiO_2$-$NaAlO_2$, Geochim. Cosmochim Acta 60 (10) (1996) 1727–1737.
[32] D. Manara, A. Grandjean, D.R. Neuville, Advances in understanding the structure of borosilicate glasses: a Raman spectroscopy study, Am. Mineral. 94 (5–6) (2009) 777–784.
[33] D. Massiot, F. Fayon, M. Capron, I. King, S.Le Calvé, B. Alonso, J.O. Durand, B. Bujoli, Z. Gan, G. Hoatson, Modelling one-and two-dimensional solid-state NMR spectra, Mag. Reson. Chem. 40 (1) (2002) 70–76.
[34] G.L. Caër, R.A. Brand, General models for the distributions of electric field gradients in disordered solids, J. Physics: Cond. Matter 10 (47) (1998) 10715–10774.
[35] J.P. Amoureux, C. Fernandez, S. Steuernagel, Z filtering in MQMAS NMR, J. Mag. Reson. A 123 (1) (1996) 116–118.
[36] J. Trebosc, B. Hu, J.P. Amoureux, Z. Gan, Through-space R3-HETCOR experiments between spin-1/2 and half-integer quadrupolar nuclei in solid-state NMR, J. Mag. Reson. 186 (2) (2007) 220–227.
[37] G. Tricot, J. Trébosc, F. Pourpoint, R. Gauvin, L. Delevoye, Chapter four - the D-HMQC MAS-NMR technique: an efficient tool for the editing of through-space correlation spectra between quadrupolar and spin-1/2 (31P, 29Si, 1H, 13C) nuclei, in: G.A. Webb (Ed.), Annual Reports on NMR Spectroscopy, Academic Press2014, pp. 145–184.
[38] G. Tricot, B. Raguenet, G. Silly, M. Ribes, A. Pradel, H. Eckert, P–O–B3 linkages in borophosphate glasses evidenced by high field $^{11}B/^{31}P$ correlation NMR, Chem. Comm. 51 (45) (2015) 9284–9286.
[39] K.J. Oh, M.L. Klein, A general purpose parallel molecular dynamics simulation program, Comp. Phys. Comm. 174 (7) (2006) 560–568.
[40] A. Tilocca, A.N. Cormack, N.H. de Leeuw, The structure of bioactive silicate glasses: new insight from molecular dynamics simulations, Chem. Mater. 19 (1) (2007) 95–103.
[41] B. Stevensson, Y. Yu, M. Edén, Structure–composition trends in multicomponent borosilicate-based glasses deduced from molecular dynamics simulations with improved B–O and P–O force fields, Phys. Chem. Chem. Phys. 20 (12) (2018) 8192–8209.
[42] A. Pedone, E. Gambuzzi, M.C. Menziani, Unambiguous description of the oxygen environment in multicomponent aluminosilicate glasses from $^{17}O$ solid state NMR computational spectroscopy, J. Phys. Chem. C 116 (27) (2012) 14599–14609.
[43] A. Pedone, Properties calculations of silica-based glasses by atomistic simulations techniques: a review, J. Phys. Chem. C 113 (49) (2009) 20773–20784.
[44] A.S. Standard, Standard Practices For Measurement of Liquidus Temperature of Glass By the Gradient Furnace method, Annual Book of ASTM Standards, American Society for Testing and Materials, Gaithersburg, 1990, pp. C829–C881.

[45] C.Le Losq, D.R. Neuville, P. Florian, G.S. Henderson, D. Massiot, The role of $Al^{3+}$ on rheology and structural changes in sodium silicate and aluminosilicate glasses and melts, Geochim. Cosmochim. Acta 126 (2014) 495–517.
[46] F.L. Galeener, Planar rings in glasses, Solid State Commun. 44 (7) (1982) 1037–1040.
[47] C.Le Losq, D.R. Neuville, W. Chen, P. Florian, D. Massiot, Z. Zhou, G.N. Greaves, Percolation channels: a universal idea to describe the atomic structure and dynamics of glasses and melts, Sci. Rep. 7 (1) (2017) 16490.
[48] A. Deshkar, O. Gulbiten, R.E. Youngman, J.C. Mauro, A. Goel, Why does $B_2O_3$ suppress nepheline ($NaAlSiO_4$) crystallization in sodium aluminosilicate glasses? Phys. Chem. Chem. Physics 22 (16) (2020) 8679–8698.
[49] P. McMillan, Structural studies of silicate glasses and melts—Applications and limitations of Raman spectroscopy, Am. Mineral. 69 (7–8) (1984) 622–644.
[50] P. McMillan, B. Piriou, A. Navrotsky, A Raman spectroscopic study of glasses along the joins silica-calcium aluminate, silica-sodium aluminate, and silica-potassium aluminate, Geochim. Cosmochim. Acta 46 (11) (1982) 2021–2037.
[51] B.N. Meera, J. Ramakrishna, Raman spectral studies of borate glasses, J. Non-Cryst. Solids 159 (1–2) (1993) 1–21.
[52] A.N. Novikov, D. Neuville, L. Hennet, Y. Gueguen, D. Thiaudière, T. Charpentier, P. Florian, Al and Sr environment in tectosilicate glasses and melts: viscosity. Raman and NMR Investigation, 2016.
[53] E.I. Morin, J. Wu, J.F. Stebbins, Modifier cation (Ba, Ca, La, Y) field strength effects on aluminum and boron coordination in aluminoborosilicate glasses: the roles of fictive temperature and boron content, Appl. Phys. A 116 (2) (2014) 479–490.
[54] J. Wu, J.F. Stebbins, Effects of cation field strength on the structure of aluminoborosilicate glasses: high-resolution $^{11}B$, $^{27}Al$ and $^{23}Na$ MAS NMR, J. Non-Cryst. Solids 355 (9) (2009) 556–562.
[55] E.M. Pierce, L.R. Reed, W.J. Shaw, B.P. McGrail, J.P. Icenhower, C.F. Windisch, E. A. Cordova, J. Broady, Experimental determination of the effect of the ratio of B/Al on glass dissolution along the nepheline ($NaAlSiO_4$)–malinkoite ($NaBSiO_4$) join, Geochim. Cosmochim. Acta 74 (9) (2010) 2634–2654.
[56] A. Winterstein-Beckmann, D. Moencke, D. Palles, E.I. Kamitsos, L. Wondraczek, Raman spectroscopic study of structural changes induced by micro-indentation in low alkali borosilicate glasses, J. Non-Cryst. Solids 401 (2014) 110–114.
[57] T. Yano, N. Kunimine, S. Shibata, M. Yamane, Structural investigation of sodium borate glasses and melts by Raman spectroscopy.: I. Quantitative evaluation of structural units, J. Non-Cryst. Solids 321 (3) (2003) 137–146.
[58] D. Manara, A. Grandjean, D. Neuville, Advances in understanding the structure of borosilicate glasses: a Raman spectroscopy study, Am. Mineral. 94 (5–6) (2009) 777–784.
[59] Y. Lai, Y. Zeng, X. Tang, H. Zhang, J. Han, H. Su, Structural investigation of calcium borosilicate glasses with varying Si/Ca ratios by infrared and Raman spectroscopy, RSC Adv 6 (96) (2016) 93722–93728.
[60] J.-P. Amoureux, C. Fernandez, S. Steuernagel, ZFiltering in MQMAS NMR, J. Mag. Reson. A 123 (1) (1996) 116–118.
[61] S.K. Lee, J.F. Stebbins, The distribution of sodium ions in aluminosilicate glasses: a high-field Na-23 MAS and 3Q MAS NMR study, Geochim. Cosmochim. Acta 67 (9) (2003) 1699–1709.
[62] X. Xue, J.F. Stebbins, $^{23}Na$ NMR chemical shifts and local Na coordination environments in silicate crystals, melts and glasses, Phys. Chem. Minerals 20 (5) (1993) 297–307.
[63] A. Quintas, T. Charpentier, O. Majerus, D. Caurant, J.L. Dussossoy, P. Vermaut, NMR study of a rare-earth aluminoborosilicate glass with varying CaO-to-$Na_2O$ ratio, Appl. Mag. Res. 32 (4) (2007) 613–634.
[64] K.J. MacKenzie, M.E. Smith, Multinuclear Solid-State Nuclear Magnetic Resonance of Inorganic Materials, Elsevier, 2002.
[65] R.E. Youngman, J.W. Zwanziger, Multiple boron sites in borate glass detected with dynamic angle spinning nuclear magnetic resonance, J. Non-Cryst. Solids 168 (3) (1994) 293–297.
[66] S. Kroeker, J.F. Stebbins, Three-coordinated boron-11 chemical shifts in borates, Inorg. Chem. 40 (24) (2001) 6239–6246.
[67] L.-S. Du, J.F. Stebbins, Nature of silicon−boron mixing in sodium borosilicate glasses: A high-resolution $^{11}B$ and $^{17}O$ NMR study, J. Phys. Chem. B 107 (37) (2003) 10063–10076.
[68] H. Bradtmuller, T. Uesbeck, H. Eckert, T. Murata, S. Nakane, H. Yamazaki, Structural origins of crack resistance on magnesium aluminoborosilicate glasses studied by solid-state NMR, J. Phys. Chem. C 123 (24) (2019) 14941–14954.
[69] M. Ren, J.Y. Cheng, S.P. Jaccani, S. Kapoor, R.E. Youngman, L. Huang, J. Du, A. Goel, Composition – structure – property relationships in alkali aluminosilicate glasses: a combined experimental – computational approach towards designing functional glasses, J. Non-Cryst. Solids 505 (2019) 144–153.
[70] M. Fortino, A. Berselli, N. Stone-Weiss, L. Deng, A. Goel, J.C. Du, A. Pedone, Assessment of interatomic parameters for the reproduction of borosilicate glass structures via DFT-GIPAW calculations, J. Am. Ceram. Soc. 102 (12) (2019) 7225–7243.
[71] N.L. Bowen, The binary system: $na_2Al_2Si_2O8$ (Nephelite, Carnegieite) - $CaAl_2Si_2O_8$ (Anorthite), Am. J. Sci. 33 (1912) 551–573.
[72] G. Lusvardi, G. Malavasi, L. Menabue, M.C. Menziani, A. Pedone, U. Segre, A computational tool for the prediction of crystalline phases obtained from controlled crystallization of glasses, J. Phys. Chem. B 109 (46) (2005) 21586–21592.
[73] A. Brehault, D. Patil, H. Kamat, R.E. Youngman, L.M. Thirion, J.C. Mauro, C. L. Corkhill, J.S. McCloy, A. Goel, Compositional dependence of solubility/retention of molybdenum oxides in aluminoborosilicate-based model nuclear waste glasses, J. Phys. Chem. B 122 (5) (2018) 1714–1729.
[74] M.J. Toplis, S.C. Kohn, M.E. Smith, I.J.F. Poplett, Fivefold-coordinated aluminum in tectosilicate glasses observed by triple quantum MAS NMR, Am. Mineral. 85 (10) (2000) 1556–1560.
[75] Q. Qin, N. Stone-Weiss, T. Zhao, P. Mukherjee, J. Ren, J.C. Mauro, A. Goel, Insights into the mechanism and kinetics of dissolution of aluminoborosilicate glasses in acidic media: impact of high ionic field strength cations, Acta Mater. 242 (2023) 118468.
[76] J. Wu, J.F. Stebbins, Cation Field Strength Effects on boron coordination in binary borate glasses, J. Am. Ceram. Soc. 97 (9) (2014) 2794–2801.
[77] M. Hubert, A.J. Faber, On the structural role of boron in borosilicate glasses, Phys. Chem. Glasses 55 (3) (2014) 136–158.
[78] N. Bisbrouck, M. Micoulaut, J.M. Delaye, M. Bertani, T. Charpentier, S. Gin, F. Angeli, Influence of magnesium on the structure of complex multicomponent silicates: insights from molecular simulations and neutron scattering experiments, J. Phys. Chem. B 125 (42) (2021) 11761–11776.
[79] N. Bisbrouck, M. Bertani, F. Angeli, T. Charpentier, D. de Ligny, J.-M. Delaye, S. Gin, M. Micoulaut, Impact of magnesium on the structure of aluminoborosilicate glasses: a solid-state NMR and Raman spectroscopy study, J. Am. Ceram. Soc. 104 (9) (2021) 4518–4536.
[80] L.S. Du, J.F. Stebbins, Solid-state NMR study of metastable immiscibility in alkali borosilicate glasses, J. Non-Cryst. Solids 315 (3) (2003) 239–255.
[81] L.-S. Du, J.F. Stebbins, Site preference and Si/B mixing in mixed-alkali borosilicate glasses: a high-resolution $^{11}B$ and $^{17}O$ NMR study, Chem. Mater. 15 (20) (2003) 3913–3921.
[82] D. Möncke, G. Tricot, A. Winterstein-Beckmann, L. Wondraczek, E.I. Kamitsos, On the connectivity of borate tetrahedra in borate and borosilicate glasses, Phys. Chem. Glasses 56 (5) (2015) 203–211.
[83] D. Möncke, G. Tricot, A. Winterstein, D. Ehrt, E.I. Kamitsos, Preferential bonding in low alkali borosilicate glasses, Phys. Chem. Glasses 58 (4) (2017) 171–179.
[84] J. Schneider, V.R. Mastelaro, H. Panepucci, E.D. Zanotto, $^{29}Si$ MAS–NMR studies of $Q^n$ structural units in metasilicate glasses and their nucleating ability, J. Non-Cryst. Solids 273 (1–3) (2000) 8–18.
[85] E.D. Zanotto, J.E. Tsuchida, J.F. Schneider, H. Eckert, Thirty-year quest for structure-nucleation relationships in oxide glasses, Int. Mater. Rev. 60 (7) (2015) 376–391.
[86] H. Bradtmüller, A. Gaddam, H. Eckert, E.D. Zanotto, Structural rearrangements during sub-Tg relaxation and nucleation in lithium disilicate glass revealed by a solid-state NMR and MD strategy, Acta Mater. 240 (2022) 118318.
[87] P. Lu, Y. Zan, J. Ren, T. Zhao, K. Xu, A. Goel, Structure and crystallization behavior of phosphorus-containing nepheline ($NaAlSiO_4$) based sodium aluminosilicate glasses, J. Non-Cryst. Solids 560 (2021) 120719.
[88] P. Lu, S. Kapoor, L. Kobera, J. Brus, A. Goel, Structural dependence of crystallization in phosphorus-containing sodium aluminoborosilicate glasses, J. Am. Ceram. Soc. 105 (4) (2022) 2556–2574.
[89] J. Wu, J.F. Stebbins, Temperature and modifier cation field strength effects on aluminoborosilicate glass network structure, J. Non-Cryst. Solids 362 (2013) 73–81.
[90] D. Ganapathi, D. Chakrabarti, A.K. Sood, R. Ganapathy, Structure determines where crystallization occurs in a soft colloidal glass, Nature Phys. 17 (1) (2021) 114–120.
[91] S. Batzner, A. Musaelian, L. Sun, M. Geiger, J.P. Mailoa, M. Kornbluth, N. Molinari, T.E. Smidt, B. Kozinsky, E(3)-equivariant graph neural networks for data-efficient and accurate interatomic potentials, Nature Comm. 13 (1) (2022) 2453.
[92] H. Wang, L. Zhang, J. Han, W. E, DeePMD-kit: a deep learning package for many-body potential energy representation and molecular dynamics, Comp. Phys. Comm. 228 (2018) 178–184.
[93] A.P. Bartók, M.C. Payne, R. Kondor, G. Csányi, Gaussian approximation potentials: the accuracy of quantum mechanics, without the electrons, Phys. Rev. Lett. 104 (13) (2010) 136403.
[94] S. Urata, Modeling short-range and three-membered ring structures in lithium borosilicate glasses using a machine-learning potential, J. Phys. Chem. C 126 (50) (2022) 21507–21517.
[95] S. Urata, N. Nakamura, K. Aiba, T. Tada, H. Hosono, How fluorine minimizes density fluctuations of silica glass: molecular dynamics study with machine-learning assisted force-matching potential, Mater. Des. 197 (2021) 109210.
[96] A. Laio, M. Parrinello, Escaping free-energy minima, Proc. Nat. Acad. Sci. 99 (20) (2002) 12562–12566.
[97] F. Lodesani, F. Tavanti, M.C. Menziani, K. Maeda, Y. Takato, S. Urata, A. Pedone, Exploring the crystallization path of lithium disilicate through metadynamics simulations, Phys. Rev. Mater. 5 (7) (2021) 075602.
[98] F. Lodesani, M.C. Menziani, S. Urata, A. Pedone, Biasing crystallization in fused silica: an assessment of optimal metadynamics parameters, J. Chem. Phys. 156 (19) (2022) 194501.